Green Chemical Engineering 4 (2023) 99–114

Contents lists available at ScienceDirect

Green Chemical Engineering

journal homepage: www.keaipublishing.com/en/journals/green-chemical-engineering

Article

A study on monoterpenoid-based natural deep eutectic solvents

Sara Rozas [a], Lorena Zamora [a], Cristina Benito [a], Mert Atilhan [b,*], Santiago Aparicio [a,*]

[a] Department of Chemistry, University of Burgos, Burgos, 09001, Spain
[b] Department of Chemical and Paper Engineering, Western Michigan University, Kalamazoo, MI, 49008-5462, USA

HIGHLIGHTS

- Low viscous, low-cost, natural monoterpenoid-based deep eutectic solvents are developed.
- Fluids were in silico and experimentally characterized.
- Low biological and environmental impact.
- Nanostructured fluids with extensive hydrogen bonding.
- Hydrophobic and low cost materials.

GRAPHICAL ABSTRACT

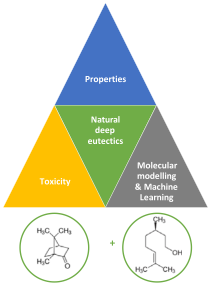

ARTICLE INFO

Keywords:
Natural deep eutectic solvents
Terpenes
DFT
MD
COSMO-RS
CO_2 solubility

ABSTRACT

Herein, the synthesis and characterization methods of natural deep eutectic solvents based on monoterpenoids have been presented. Low viscous fluids with suitable physicochemical properties are produced. The materials are non-toxic, biodegradable, and cost-effective. Thus, they can be used to develop sustainable solvents for various processes and can find their applications in various fields. A theoretical study based on quantum chemistry and classical molecular dynamics is used for the nanoscopic characterization of structure, dynamics, and hydrogen bonding. The reported results help analyze the properties of this new family of solvents. The required information for developing structure–property relationships for proper solvent design to form a sustainable chemistry framework is obtained.

1. Introduction

Abbott et al. [1] were the first to publish an article in 2001 describing the formation of a liquid mixture at room temperature. The mixture was prepared by mixing quaternary ammonium salts and metal chloride salts. Deep eutectic solvents (DESs) have emerged as a potential green alternative to the ionic liquid (IL) predecessors and traditional volatile organic compounds (VOCs) [2]. DESs are a mixtures of two or more components and are prepared by mixing the components in suitable molar ratios. Under these conditions, a large decrease in the melting point is achieved. The melting point of the mixture is lower than those of the individual components [3]. Based on the nature of the mixed components, the DESs are classified into five main categories [3–5]: Type I, quaternary ammonium salts (QASs) + metal chloride; Type II, QASs + metal chloride hydrate; Type III, QASs (acting as hydrogen bond acceptors, HBAs) + hydrogen bond donors (HBDs) [6,7]; Type IV, metal chloride hydrate + HBDs [8,9]; Type V, formed by mixing non-ionic compounds [10]. The large melting point depression is explained, especially for the Types III and V DESs, by the strong hydrogen bonding interactions between the mixed components (HBAs and HBDs) [11,12].

The nature of the compounds used for developing DESs determines their properties. For Type III and Type V DESs, compounds of natural

* Corresponding author.
E-mail addresses: mert.atilhan@wmich.edu (M. Atilhan), sapar@ubu.es (S. Aparicio).

https://doi.org/10.1016/j.gce.2022.05.005
Received 24 March 2022; Received in revised form 9 May 2022; Accepted 20 May 2022
Available online 24 May 2022

origin have been proposed as starting materials, and these are used for the formation of the so-called natural DESs (NADESs) [13–15], which are characterized by low toxicity, biodegradability, and low production costs. Thus, DESs are suitable for the development of a sustainable chemistry framework [16]. It is well-known that the water content plays a pivotal role in the structure and properties of DESs/NADESs [17,18]. Thus, hydrophobic or hydrophilic ones can be potentially considered [19]. Therefore, the physicochemical properties of DESs strongly depend on the nature of HBA/HBD combinations, molar ratio, water content, and temperature [20]. This highlights the possibility of designing natural solvents with tailored features. The characteristics of DESs/NADESs that can be used as designer solvents have attracted the interest of researchers working in industries and academia [21]. NADESs are non-toxic, fully biodegradable, less volatile, cost-effective materials that exhibit suitable physicochemical properties that make them appropriate alternative materials for ILs [22] and VOCs [23]. Therefore, it has been proposed that DESs/NADESs can be used in different fields such as the pharmaceutical industry [24], catalytic processes [25], electrochemistry [26], gas separation [27], and extraction operations [28].

NADESs have attracted attention as particular attention is currently being paid to developing greener and sustainable alternatives to the currently used solvents in the industry [29]. Therefore, the use of different naturally occurring compounds such as HBD/HBA molecules has been considered [30]. These molecules include organic acids, amino acids, terpenes, sugars, alcohols, etc. Terpenes are versatile natural compounds that are extracted from plants and essential oils obtained from trees [31]. These have been used in the last few years to study NADES. The materials have been particularly used in the pharmacological field as a vehicle for drug delivery [32]. These have also been used for anticancer therapy [33] and as antimicrobial agents [24]. Among the terpene families, monoterpenoids consist of two linked isopropene units (C_{10} chains) [34]. Some of the compounds can be used to synthesize cyclic structures, or they can be oxidized in various ways [35]. Because of their biological properties (antimicrobial, anti-inflammatory, antioxidative, anti-mutagenic, analgesic, and sedative) [24], monoterpenoids have been widely studied in the medical field. Abdallah et al. [34] studied the physicochemical properties of four monoterpene-based NADES (menthol-borneol, thymol-borneol, menthol-camphor, and thymol-camphor). They used theoretical and experimental methods to study the hydrogen bonding interactions in the eutectic system. Li et al. [36] experimentally characterized various hydrophobic monoterpene-based NADES, thymol-menthol, and thymol-camphor, for antibiotic analysis. Through molecular dynamics simulations and quantum mechanics calculations, Fan et al. [37] theoretically studied the viscosity of menthol-citronellol and thymol-citronellol based DES based on the hydrogen bonding interactions present in the systems. Rodrigues et al. [38] also experimentally studied the menthol-camphor and menthol-thymol NADES systems revealing their potential to inhibit the development of colorectal cancer cells. NADESs composed solely of monoterpenoids have rarely been studied. Details of the physicochemical properties and nanoscopic behavior, including hydrogen bonding, of these systems are not reported in the literature. Therefore, it is necessary to develop a systematic analysis method to study the physicochemical properties of the monoterpenoid-based HBA-HBD combinations to design NADES systems.

We selected eight monoterpenoids to design natural DESs among which. These consisted of five HBA and three HBD (camphor (CAMPH), 1,8-cineole (CN), carvone (CARV), citronellal (CILLAL), and citral geranial (CIT) as HBAs; and linalool (LIN), citronellol (CILLOL) and geraniol (GER), as HBDs; Fig. 1a). Fifteen different NADESs were considered in this work: CAMPH-LIN, CAMPH-CILLOL, CAMPH-GER, CN-LIN, CN-CILLOL, CN-GER, CARV-LIN, CARV-CILLOL, CARV-GER, CILLAL-LIN, CILLAL-CILLOL, CILLAL-GER, CIT-LIN, CIT-CILLOL, and CIT-GER. The HBA:HBD molar ratio was 1:1 for all the systems.

The purpose of this work is to theoretically design and experimentally prepare fifteen different monoterpenoid-based NADES and extensively characterize their properties at the nano-and microscale. We also aimed to realize detailed macroscopic physicochemical characterization. The aim was to effectively study the structure–property relationships (Fig. 1b). Theoretical characterization was done considering short-range interactions using the density functional theory (DFT) technique. The liquid phase properties were analyzed using classical molecular dynamics (MD) simulation methods. Particular attention was paid to understanding the hydrogen bonding interactions and their relationships with the properties of the monoterpenoid-NADES systems. The use of molecular modeling methods (primarily DFT and MD) for DES design and characterization has proved to be a rapidly evolving research field. These techniques can be used to effectively study the fundamental questions on DESs [39,40]. These theoretical studies have unveiled the effect of hydrogen bonding interactions on the properties and structure of DESs [41,42]. Molecular-level features such as gas solubility [43], design of pharmaceutical compounds [44], nanomaterial properties [45], fuel recovery ability [46], and water effect on DESs properties [47] were studied using relevant technologies. Nevertheless, most of the available molecular modeling studies have been used to study traditional DESs. Studies on NADESs are scarce [48]. Therefore, theoretical studies reported in this work will contribute to the nanoscopic characterization of new types of NADES. The results can be obtained using molecular simulation tools. Likewise, the development of predictive methods for the prediction of relevant physicochemical properties of DES/NADES is of great relevance considering the large number of possible fluids that can be developed. Machine learning (ML)-based methods have been used by researchers [49,50] to study these systems. These methods have also been used to study NADES [51]. Therefore, we developed ML methods to predict the relevant properties of the considered monoterpenoid-based NADESs.

An experimental study was carried out on the thermophysical properties of the designed NADES. This is the first report where a combination of experimental and theoretical methods was used to study the monoterpenoid-based NADES. The physicochemical properties and structuring of fifteen type V DESs are described, and the behaviors of novel type V NADESs are discussed.

2. Materials and methods

2.1. Chemicals

The pure chemicals used to develop NADES were obtained from commercial sources. The purities are reported in Table S1 (Supplementary Information). The fifteen different NADESs were prepared by combining five HBAs and three HBDs in a 1:1 (HBA:HBD) molar ratio (Figs. 1 and S1 (Supplementary Information)). NADES was prepared following the weighing procedure (Mettler AT261 balance, $\pm 1 \times 10^{-5}$ g), using suitable amounts of each compound. The components were stirred under heating conditions at 40 °C. Liquid samples were dried under vacuum using a Heidolph rotary evaporator at 40 °C. Transparent and colorless liquid samples were obtained (Fig. S1, Supplementary Information), which remained in the liquid state at 20 and 0 °C. The large liquid window range was studied (Table S2 (Supplementary Information)). The water content of the samples used in this work was measured using a Karl-Fischer coulometric titrator (Metrohm 831 KF coulometer,

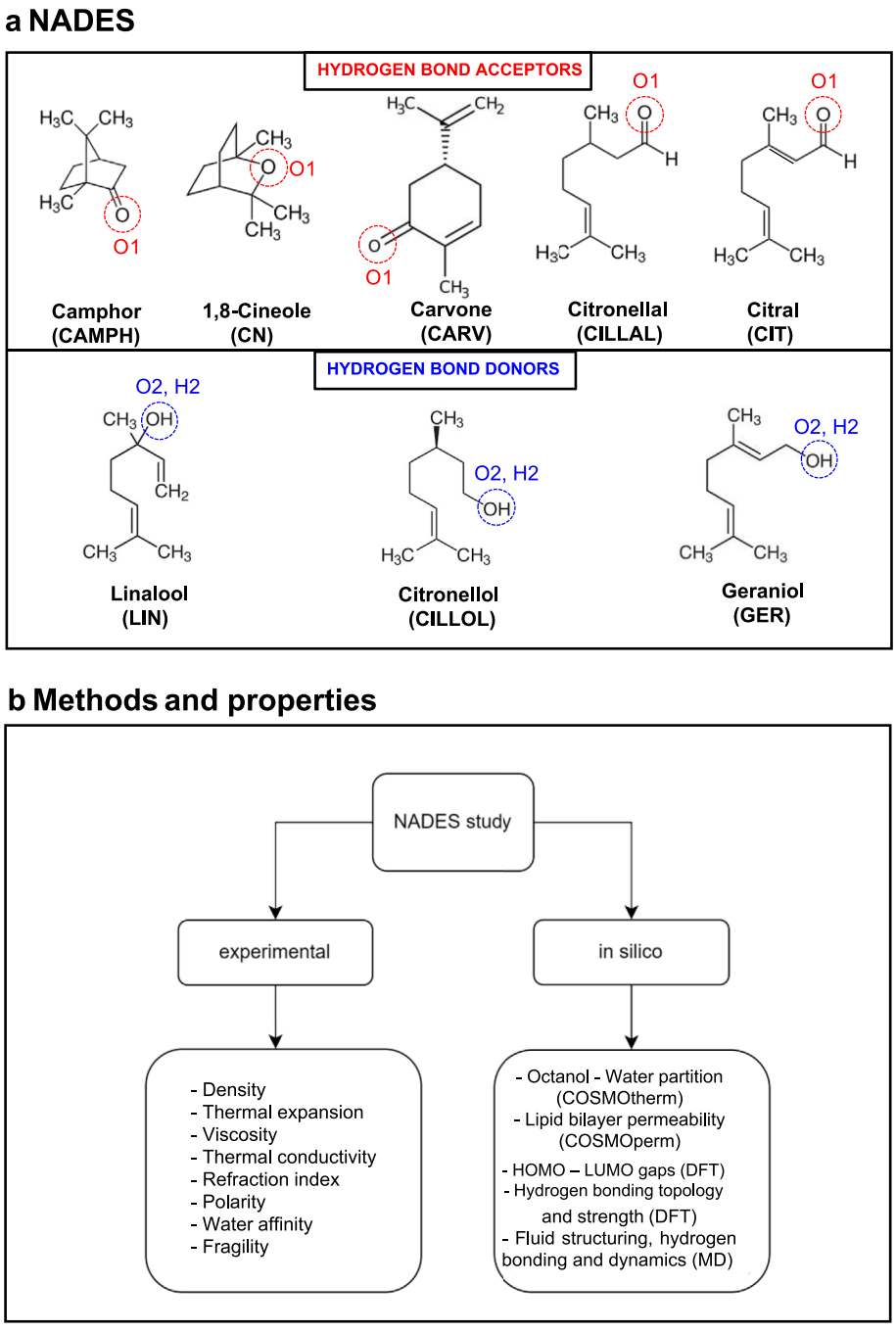

Fig. 1. (a) Monoterpenoid molecules considered in this work for the development of NADES using a combination of the indicated HBDs and HBAs. Hydrogen bonding sites as well as atom labeling used in this work are indicated in red and blue dashed lines. (b) Experimental and in-silico properties considered in this work.

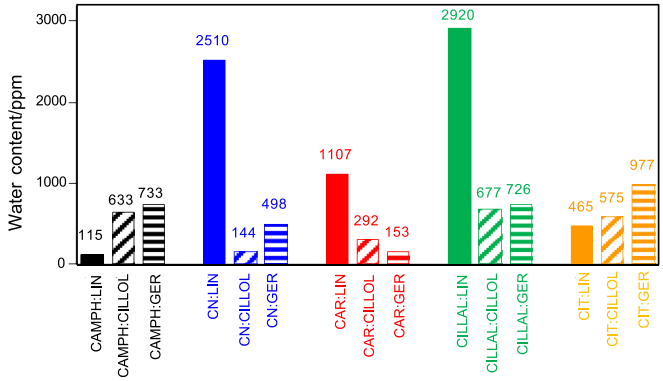

Fig. 2. Water content of the NADESs considered in this work (HBA:HBD = 1:1, mole ratio).

±0.3%). Samples with low water content (< 0.3 wt%) were considered in this work (Fig. 2). Samples were kept and handled under vacuum to avoid water absorption.

2.2. Apparatus and procedures

Selected and relevant physicochemical properties (density, shear viscosity, thermal conductivity, refractive index, and Reichardt's polarity parameter) are studied in this work. These properties were studied in the temperature range of 293–333 K. The refraction index was determined at the temperature of 323 K. Density (ρ) was measured using an Anton Paar DMA1001 (uncertainty 1×10^{-4} g cm^{-3}) vibrating tube densimeter. The cell temperature was controlled and measured using a built-in internal

Peltier (uncertainty 0.01 K). The changes in the density of the samples with temperature followed a linear trend for all the considered NADESs ($R^2 > 0.9999$). The thermal expansion coefficient, α_p, was calculated as follows:

$$\alpha_p = -\frac{1}{\rho}\left(\frac{\partial \rho}{\partial T}\right)_p = -\frac{1}{\rho}a \quad (1)$$

where a is the slope of the ρ *vs.* temperature linear fit plot.

To study the shear viscosity (η), an electromagnetic VINCI Tech EV1000 viscometer [52] was used (uncertainty 2%). The system was coupled with a constant-temperature circulating bath (Julabo Presto) for temperature control. The temperature was measured in the cell using a platinum resistance thermometer (PRT, ±0.01 K). The measured η (as a function of temperature) did not follow Arrhenius behavior, and hence the data were fitted to the Vogel–Fulcher–Taman (VFT) equation as follows:

$$\eta = \eta_0 \exp\left(\frac{B}{T - T_0}\right) \quad (2)$$

VFT fitting parameters were used to calculate Angell's fragility parameter (D_f).

$$D_f = \frac{B}{T_0} \quad (3)$$

The refraction index (sodium D-line, n_D) was measured using a Leica AR600 refractometer ($\pm 1 \times 10^{-5}$) that was coupled to an external circulator (Julabo F32) for temperature control. The temperature was measured with a PRT in the cell (±0.01 K). Thermal conductivity (σ) was measured using a Decagon devices KD2 Thermal analyzer (KS-1 sensor, 6 cm long, 1.3 mm in diameter, single needle, uncertainty: 5%). The temperature was controlled using a Julabo F32 bath and measured with a PRT (±0.01 K). The properties studied are reported in Table S2 (Supplementary Information).

The polarity of the NADES system was measured using Reichardt's dye (Sigma–Aldrich, 90% purity; solvatochromic dye). Dye solutions (1×10^{-4} M) were prepared for each NADES system, and visible spectra were recorded on a LanTechnics UV-18 spectrophotometer (±0.5 nm). The cell temperature was controlled and measured using a Peltier (±0.1 K) system. The Reichardt's normalized solvatochromic parameter, E_T^N, was calculated from the maximum wavelength of the obtained spectra [53].

Table 1
Results of VFT fits experimental viscosity data, Eq. (2) in the 293.15–333.15 K temperature range. Angell's fragility parameter, D_f, was calculated from fitting coefficients as in Eq. (3).

System	η_0/(mPa s)	B/K	T_0/(mPa s)	*RMSD*	D_f
CAMPH:LIN (1:1)	0.0047	1305.6	114.3	0.02	11.4
CAMPH:CILLOL (1:1)	0.0049	1438.7	99.7	0.05	14.4
CAMPH:GER (1:1)	0.0049	1516.4	84.6	0.01	17.9
CN:LIN (1:1)	0.0044	1359.5	90.9	0.03	15.0
CN:CILLOL (1:1)	0.0050	1512.8	75.2	0.01	20.1
CN:GER (1:1)	0.0052	1530.3	61.4	0.01	24.9
CAR:LIN (1:1)	0.0041	1406.4	75.7	0.01	18.6
CAR:CILLOL (1:1)	0.0047	1535.0	68.1	0.02	22.5
CAR:GER (1:1)	0.0050	1559.4	58.7	0.01	26.6
CILLAL:LIN (1:1)	0.0043	1449.9	69.4	0.02	20.9
CILLAL:CILLOL (1:1)	0.0023	1258.3	136.4	0.05	9.2
CILLAL:GER (1:1)	0.0023	1203.9	138.7	0.06	8.7
CIT:LIN (1:1)	0.0025	1615.5	66.2	0.12	24.4
CIT:CILLOL (1:1)	0.0027	1644.7	63.3	0.01	26.0
CIT:GER (1:1)	0.0035	1744.6	41.6	0.01	41.9

2.3. Prediction of thermophysical properties using machine learning methods

Density and viscosity (Table S2, Supplementary Information) were used for developing predictive methods by using ML methods. These two thermophysical properties are pivotal for the industrial application of NADES. Considering the scarcity of experimental data for Type V NADES,

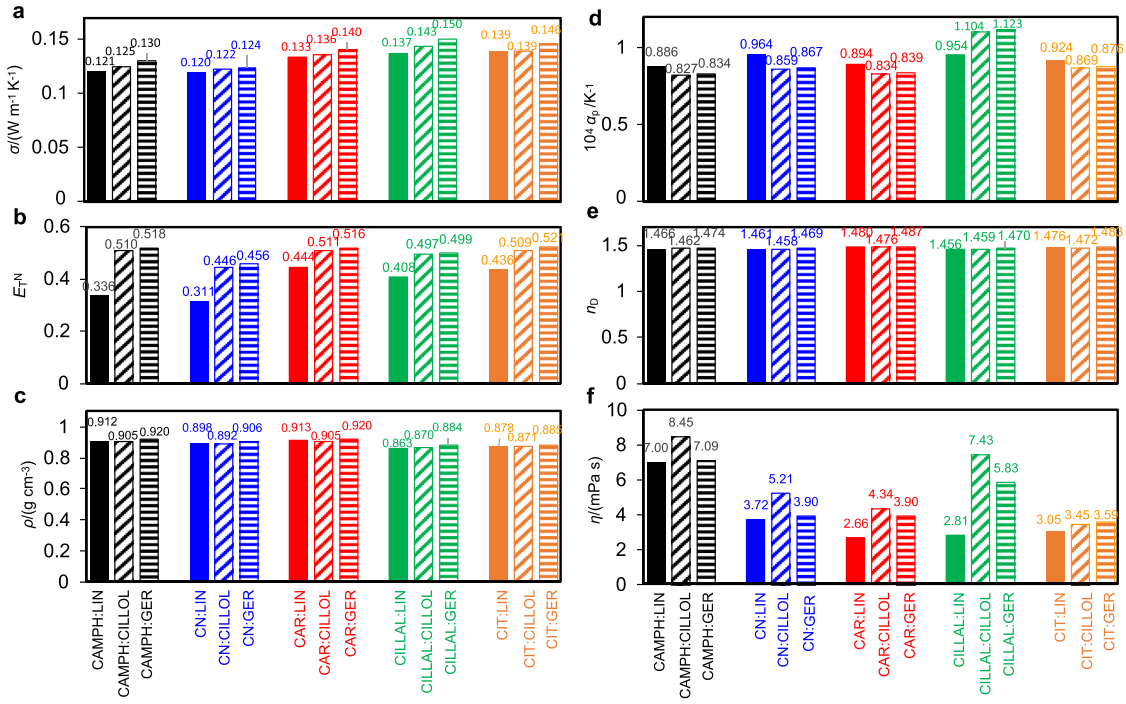

Fig. 3. Thermophysical properties of the NADESs considered in this work (HBA:HBD = 1:1, mole ratio; 293.15 K). (a) Thermal conductivity, σ, (b) Reichardt's polarity parameter, E_T^N, (c) density, ρ, (d) isobaric thermal expansion coefficient, α_p, (e) refraction index, n_D, and (f) dynamic viscosity, η.

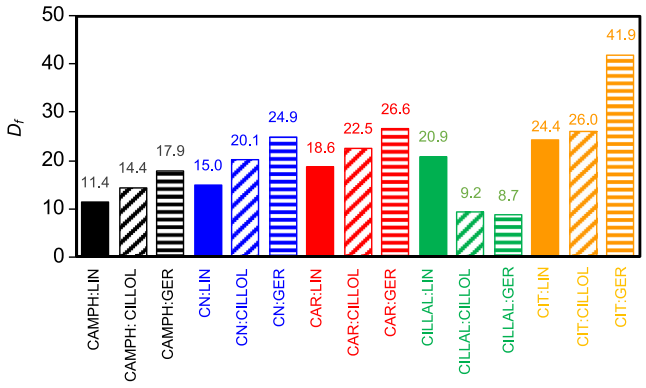

Fig. 4. Angell's fragility parameter, D_f, obtained from the VFT fitting parameters to determine the experimental viscosity (Table 1) of the NADESs considered in this work.

the development of predictive numerical methods is highly relevant. The recorded experimental data were split into the training (70%) and validation (30%) sets for use in ML methods. The developed models were based on 3D inductive molecular descriptors developed by Cherkasov [54], which were based on the optimized structures of isolated molecules (HBAs and HBDs). The DFT technique at the BP86/def-TZVP theoretical level in TmoleX [55] and the Online Chemical Database (OCHEM) Descriptor Calculator were used to develop the models [56]. Additionally, the HOMO–LUMO gaps for each compound were calculated from the DFT optimized structures. Therefore, 55 molecular descriptors were considered for each HBA/HBD system (Supplementary Information). ML calculations were carried out using MATLAB. Different ML methods were considered, including (i) linear regressions, (ii) regression trees, (iii) support vector machines (SVM), (iv) Gaussian process regression (GPR), and (v) ensembles of trees. The model which generated the lower root mean square error (RMSE) value was selected.

2.4. DFT calculations

Hydrogen bonding in the considered NADESs was first analyzed using the DFT technique using the ORCA program [57] under conditions of the B3LYP [58–60] functional, 6–311++G(d,p) basis set, and D3 [61] dispersion contribution (semiempirical Grimme's method). Avogadro [62] program was used to build the initial structures of the HBA and HBD monomers. The HBD/HBA mole ratio of 1:1 was used to develop the minimal clusters. For each HBA: HBD combination (*i.e.*, each of the 15 possible considered NADESs), the available hydrogen bond donor and acceptor sites were considered, *i.e.*, ethers, ketones, and aldehydes were the acceptor groups in HBA monomers, and alcohol was the donor group in the HBD monomers. The cluster geometries were optimized, and the interaction energies (ΔE) for all the considered structures were calculated as the difference between the energy of the cluster and the sum of the corresponding monomers. The basis set superposition error (BSSE) was corrected using the counterpoise method [63]. The topology of the hydrogen bonds was analyzed using the quantum theory of atoms in molecule (QTAIM; Bader's theory) theory [64] and the MultiWFN software [65]. Based on the principles of the QTAIM analysis method, the primary intermolecular interactions were studied using the bond (BCPs, type (3,-1) in QTAIM) and ring (RCPs, type (3,-1) in QTAIM) critical points using the corresponding electron density (ρ_e) and Laplacian of the electron density ($\nabla^2\rho_e$). Non-covalent interaction analysis (NCI [66]) and

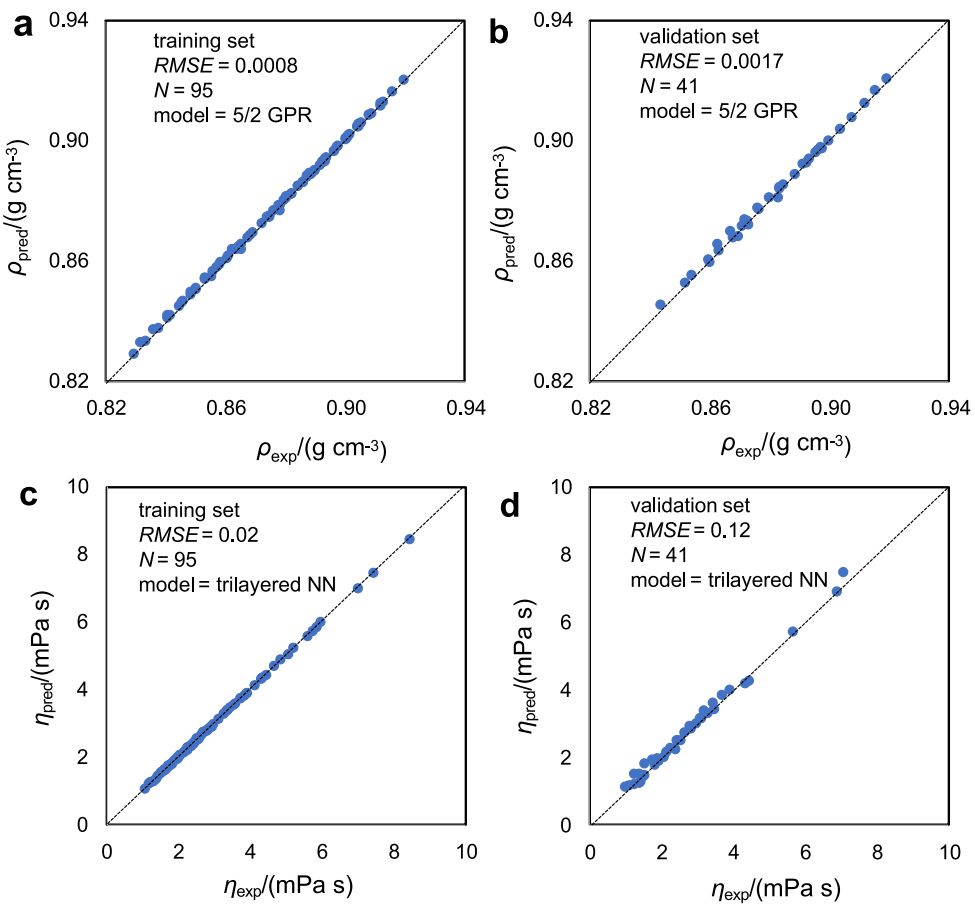

Fig. 5. Results obtained using the ML technique for (a,b) density, ρ, and (c,d) dynamic viscosity, η, prediction. Values predicted from the model (pred) and experimental (exp) data. Panels (a,c) show training sets with experimental data for the NADESs considered in this work. Panels (b,d) reveal the predictions (validation) using the developed models for the same systems. *RMSE* (root mean square error), *N* (number of data points), GPR (Gaussian Process Regression), and trilayered NN (Neural Networks).

interaction region indicator (IRI [67]) analysis methods were also developed to study the optimized clusters using MultiWFN. Hydrogen bonding was also analyzed using the electron localization function (ELF), from which the core-valence bifurcation index (CVB [68]) was calculated.

2.5. Docking calculations

Docking calculations for HBA/HBD (1:1) pairs were conducted based on the studied NADES (Fig. 1) systems. The human serum albumin (HSA) protein (PDB code 1AO6) was considered during the studies. The HSA protein has been previously considered to study the (toxicological) effects of compounds closely related to DESs, such as ILs [69]. Thus, it was selected as a suitable target to investigate the possible biological effects of the considered NADESs. The protein structure was obtained from the Protein Databank, and the target cavity for docking studies was the hydrophobic pocket in the subdomain IIA (Sudlow's site I) [69]. The structure of the protein was prepared using Autodock Tools, and the docking region was centered in the TRP214 residue ($30 \times 30 \times 30$ Å^3 boxes). The HBA/HBD pairs were optimized using the DFT technique, as mentioned in Section 2.4. Autodock Tools was also used for docking. The Gasteiger charges were considered for all the systems. Docking studies in the selected cavity were carried out using Autodock Vina [70]. The obtained docked structures were ranked based on the corresponding affinities (scores). The systems with higher ranks were selected for further analysis. The protein–ligand interaction profiler was used for the studies [71].

2.6. COSMO calculations

The DFT optimized HBA: HBD structures, as explained in Section 2.4, were subjected to conditions of single-point calculations at the BP86/def-TZVP level to calculate the COSMO files. The COSMO and COSMOperm calculations were conducted using the COSMOthermX software [72]. The COSMO files were considered to analyze the properties of the considered NADES components. These files were also used for the prediction of octanol–water partition coefficients (log(*P*)). The biological effects of the considered NADES, their behavior, and penetration abilities through cell walls (modeled as simplified lipid bilayers) were also considered. For this purpose, the COSMOperm method was used to analyze the membrane permeability of the considered HBA:HBD pairs. NADES permeation was resembled using biological lipid membranes. The 1-palmitoyl-2-oleoyl-sn--glycero-3-phosphocholine (POPC) lipid was used to model the composition of the lipid bilayers. The permeability of the considered pairs, as well as the free energy profiles for the permeation in the bilayer, was studied [73].

2.7. Classical molecular dynamics simulation

MD simulations were done using MDynaMix v.5.2 [74] software. The force field parameters used by us are presented in Table S3 (Supplementary Information). The parameters were derived from the Merck Molecular Force Field (SwissParam database [75]). The atomic charges were inferred from the ChelpG charges [76] obtained from the DFT simulations of isolated monomers. The initial cubic simulation boxes containing 1000 molecules (500 HBA molecules and 500 HBD molecules) were built using the Packmol [77] program.

MD simulations were performed following a two steps process: (i) 10 ns NVT optimization at 503 K and 1 bar. This was followed by (ii) 30 ns NPT optimization at 303 K and 1 bar for the production runs, as shown in Table S4 (Supplementary Information). The Nose-Hoover method [78] was used to control the pressure and temperature. The Tuckerman–Berne double time step algorithm [79] was used for equations of motion (1 and 0.1 fs for long-and short-time steps). The Ewald method was considered for electrostatic interactions [80] (15 Å for cut-off radius). A 15 Å cut-off distance was also considered for the Lennard–Jones interactions and Lorentz–Berthelot mixing rules for cross terms. A fully diffusive regime was assured for all the simulations by analyzing the log-log plots obtained by plotting the mean-square displacements versus simulation

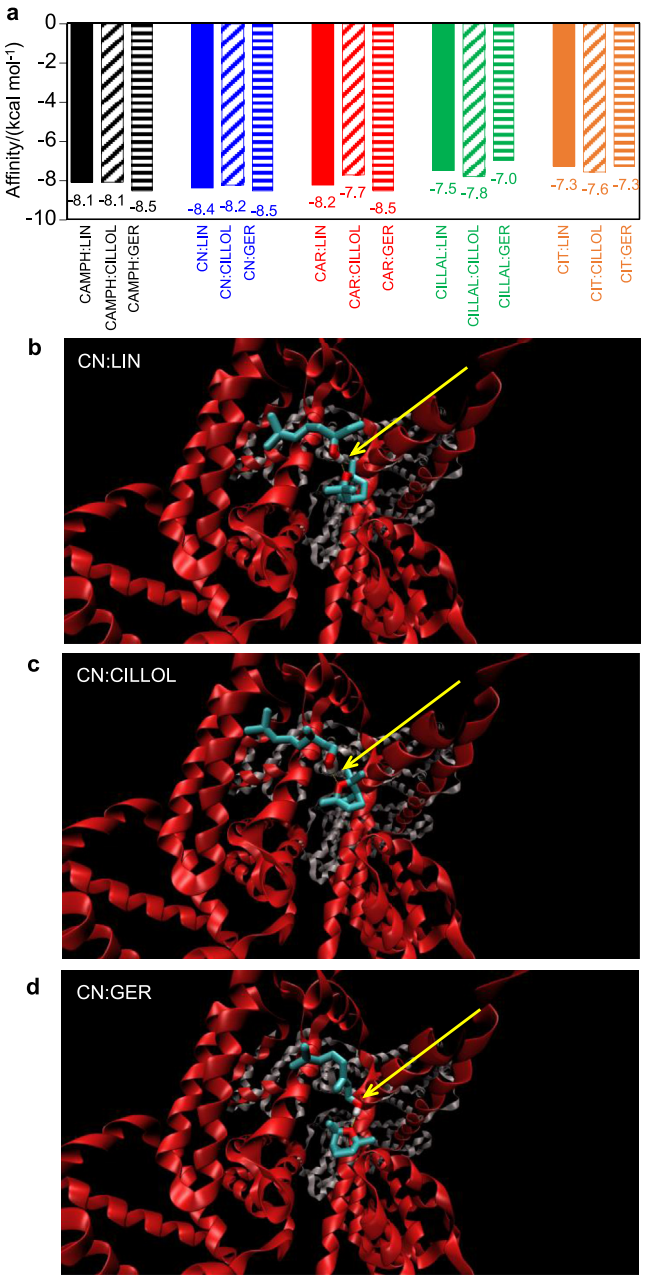

Fig. 6. (a) Results obtained for NADES docking for the 1AO6 protein (Sudlow's Site I) for the best poses indicating affinity. Panels (b to d) show CIN:LIN, CIN:CILLOL, and CIN:GER best-docked results. The color red and ribbons indicate the A and B subunits of the HSA protein.

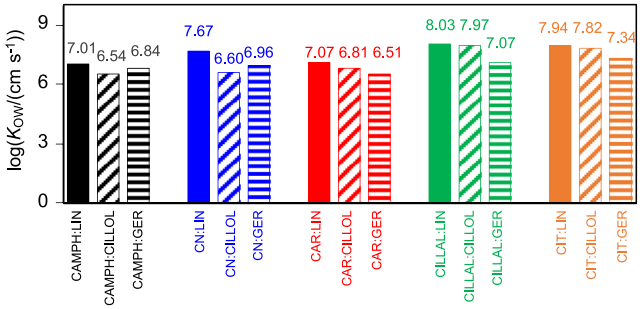

Fig. 7. Predicted (COSMOtherm) octanol–water partition coefficients, $log(K_{OW})$, at 298.15 K for the considered NADESs.

time. This resulted in slopes in the 0.98–1.00 range for all the considered NADES. The low viscosity of the considered NADES systems (< 10 MPa, Table S2, Supplementary Information) assures proper sampling with MD simulations. MD trajectories were analyzed using TRAVIS [81] and VMD [82] programs to obtain insights into the structure and dynamics of intermolecular forces.

3. Results

3.1. Experimental analysis

The physicochemical properties of the studied monoterpenoid-NADESs are reported in Table S2 (Supplementary Information) in the studied temperature range. The water content reported in Fig. 2 is remarkably low. The data reveal the hydrophobicity of the fluids. These fluids can be handled in open-air conditions without significant water sorption from atmospheric humidity. Details of the physicochemical properties studied are reported in Fig. 3.

Thermal conductivity, σ, is a relevant property that determines the applicability of the DES/NADES systems in heat transfer operations. The σ values reported in Fig. 3a are in the range of 0.12–0.15 $W\,m^{-1}\,K^{-1}$, which is lower than that recorded for other types of DES, *e.g.*, σ values for choline chloride (ChCl)–based Type III DES are larger than 0.2 $W\,m^{-1}\,K^{-1}$ [83]. These low σ values are in the range of the values recorded for some ILs such as [BMIM][PF_6] (1-butyl-3-methylimidazolium hexafluorophosphate) or common VOCs such as toluene [84]. The minor differences in the σ values recorded for the DES systems reveal that the effect of HBA and HBD is not significantly high. The significance of the roles of HBA is in the order of CAMPH ≈ CN < CAR < CILLAL ≈ CIT. This can potentially be attributed to the cyclic shape of CAMPH, CN, and CAR. The HBD effect is in the order of LIN < CILLOL < GER for a fixed HBA. This can be attributed to the position of the hydroxyl groups in the monoterpenoid molecule and the presence of double bonds, which control molecular flexibility and dynamics that affect the thermal conductivity of the system.

The polarity of the fluids quantified based on the E_T^N values are reported in Fig. 3b. A non-negligible HBA and HBD effect is exerted on this property, and the values are in the range of 0.31–0.52. This indicates that these fluids are of moderate or low polarity (*i.e.*, these NADES systems exhibit roughly 30%–70% of water polarity). The polarity of monoterpenoid-based NADES is remarkably lower than that of archetypical Type III DESs, such as ChCl–urea, ethylene glycol, or glycerol, the E_T^N values of which are approximately 0.8 [85]. Other types of ChCl-DESs, such as levulinic acid or glycolic acid, are characterized by modest polarities. The E_T^N values of these systems are approximately 0.35 [86]. The order of polarity of the NADES system is as follows:

CAMPH ≈ CN < CILLAL < CAR < CIT, and LIN < CILLOL < GER (for HBAs and HBDs, respectively). The polarities of the NADES systems should be considered when they are used for solubilization and extraction. This can potentially result in modest solubilities for predominantly polar compounds.

The data on density are reported in Fig. 3c. All fluids are less dense than water. The densities of the systems containing CAMPH, CN, and CAR were similar. CIT- and CILLAL-NADES were characterized by very low densities. The density increases in the order of LIN < CILLOL < GER. The densities of these two systems were the lowest among the densities of all the studied solvents. The temperature effect on density (Table S2, Supplementary Information) is linear for all the considered NADES systems. The negative slope results in the generation of isobaric thermal expansion coefficients (Fig. 3d). The α_p values increase linearly with temperature (Table S2, Supplementary Information) and indicate that these are compressible fluids. These fluids were more compressible than the choline chloride-based DESs, the α_p values of which were in the range of $(0.5\text{-}0.6)\times10^{-4}\,K^{-1}$ [87]. The low density and significant thermal expansion coefficients recorded for the studied NADES system indicate

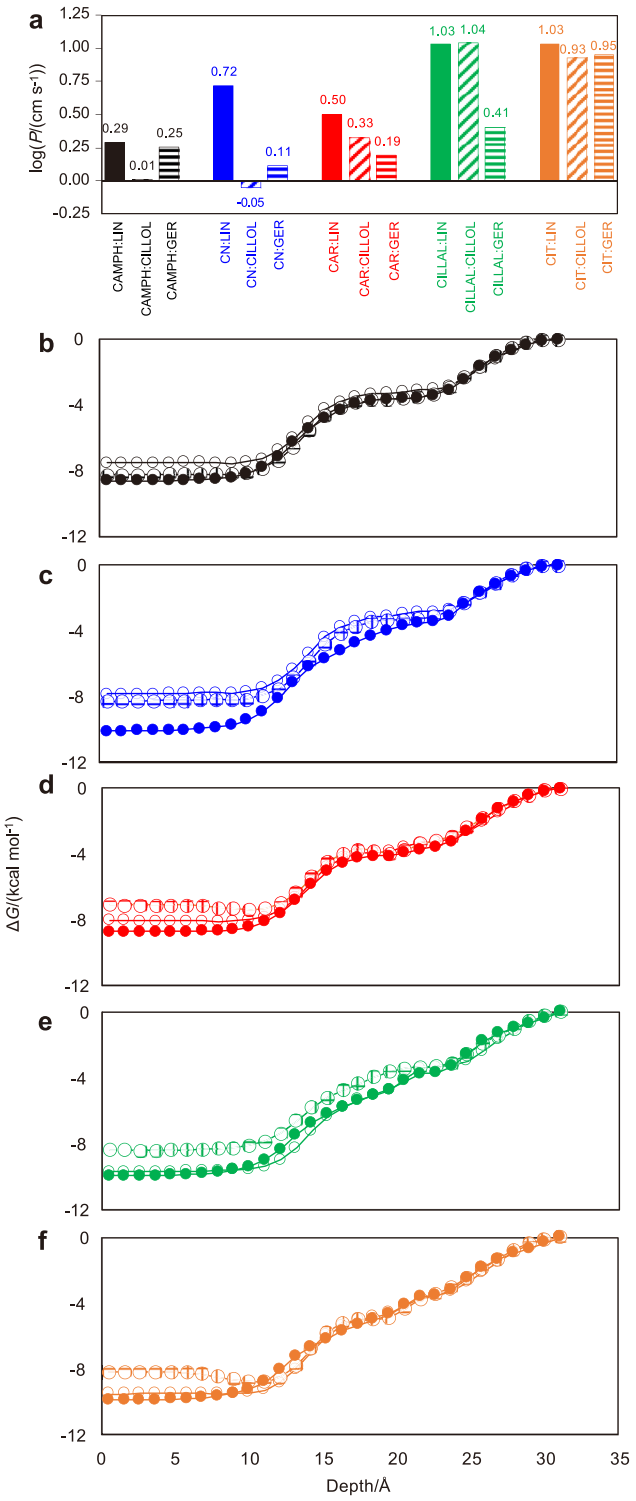

Fig. 8. COSMOperm results for the interactions between the reported NADES pairs and the POPC lipid bilayer. (a) Calculated permeability (P) and (b–f) free energy profiles, ΔG, for the penetration of the reported NADES pairs into a POPC lipid bilayer (Depth = 0 stands for the center of the bilayer).

that the fluids were characterized by a large free volume. The results were confirmed by measuring the refraction index (Fig. 3e). The reported n_D values were in the range of 1.46–1.50. Minor differences were observed for the considered HBA/HBD systems. The values decreased linearly with an increase in the temperature (Table S2, Supplementary Information). The trend was similar to the trend observed for the change

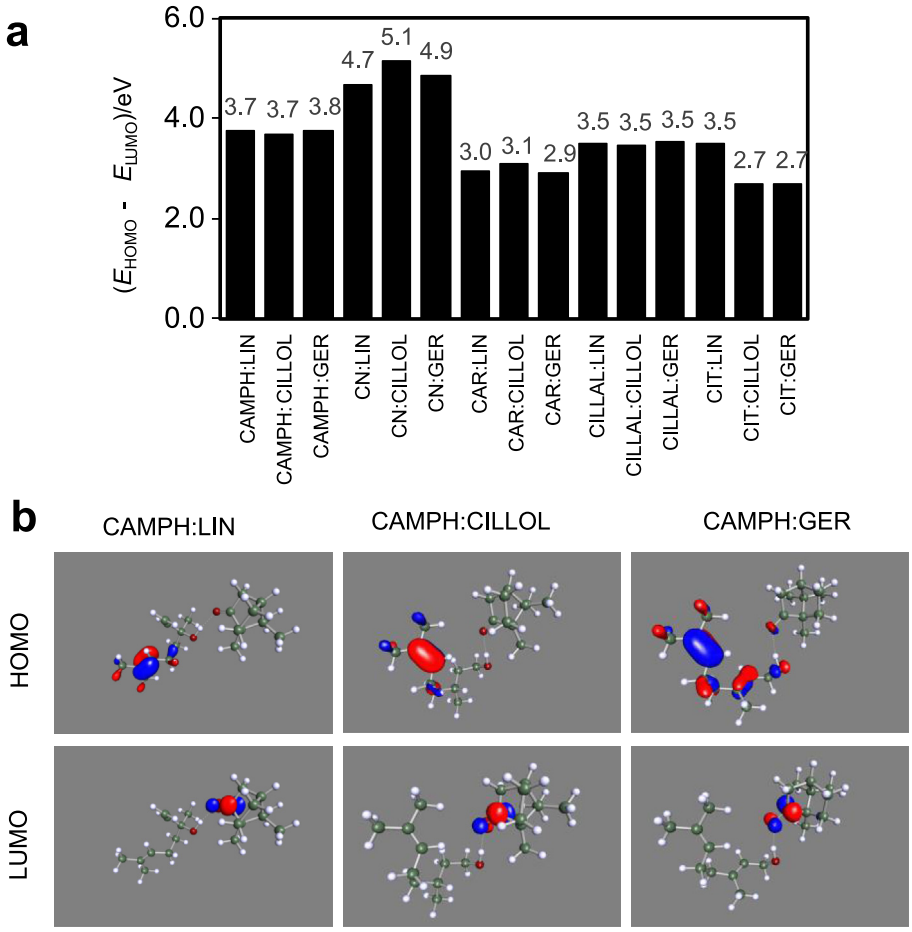

Fig. 9. (a) HOMO–LUMO energy gap for monoterpenoid-based NADES considered in this work and the (b) HOMO and LUMO orbitals of the CAMPH-based NADES obtained from DFT calculations.

in density. Slightly larger n_D values were obtained for CIT/CAR-based NADES. This agrees with the lower density values of the systems.

It is interesting that the monoterpenoid-NADES systems are characterized by low viscosity, and the viscosity of the system is lower than 8.5 mPa s. The viscosity decreases in a non-Arrhenius way with an increase in the temperature (Fig. 3f and Table S2, Supplementary Information). These low viscosity values are in the range of the viscosities of most of the common organic solvents that are considered for industrial applications. These solvents are used in fields where the properties of viscosity-controlled mass or heat diffusion are pivotal. Type III NADESs

Table 2
QTAIM analysis of (3,-1) BCPs appearing in the HBA:HBD hydrogen bonds (O–HO) reporting electron density, ρ_e, and $\nabla^2\rho_e$ at the corresponding BCP for the reported molecular clusters (HBA:HBD 1:1). Core-Valence Bifurcation (CVB) index is also reported for each hydrogen bonding. $d_{O—HO}$ stands for the distance between the H atom in the OH group of the HBD and the O atom in the HBA. ΔE stands for counterpoise corrected interaction energy. Values are obtained from DFT calculations.

Cluster	ρ_e/a.u.	$\nabla^2\rho_e$/a.u.	CVB	$d_{O—HO}$/Å	ΔE/(kJ mol^{-1})
CAMPH:LIN	0.02280	0.08706	0.02371	1.96	−19.6
CAMPH:CILLOL	0.02281	0.08666	0.02313	1.96	−20.6
CAMPH:GER	0.02155	0.08154	0.02668	1.98	−18.5
CN:LIN	0.02105	0.07814	0.02696	2.01	−17.1
CN:CILLOL	0.02462	0.09063	0.01670	1.94	−17.8
CN:GER	0.02476	0.09210	0.01761	1.94	−18.1
CAR:LIN	0.02115	0.08435	0.03222	1.97	−17.3
CAR:CILLOL	0.02331	0.08945	0.02282	1.95	−21.0
CAR:GER	0.02375	0.09201	0.02282	1.94	−20.2
CILLAL:LIN	0.02309	0.08413	0.01566	1.98	−20.2
CILLAL:CILLOL	0.02343	0.08390	0.01493	1.98	−19.7
CILLAL:GER	0.01983	0.07668	0.03259	2.01	−16.0
CIT:LIN	0.02346	0.08414	0.01536	1.97	−20.2
CIT:CILLOL	0.02594	0.09182	0.00726	1.93	−23.1
CIT:GER	0.02625	0.09399	0.00818	1.92	−21.8

are characterized by high viscosity values. This is a clear drawback that limits their application in industries [88]. The largest viscosity values were obtained for CAMPH-based NADES, and the lowest values were recorded for the LINs acting as HBDs. CILLOL results in increased viscosity, whereas GER shows intermediate behavior among LIN and CILLOL. Therefore, a fluid consisting of CAR and LIN with a viscosity of 2.66 mPa s can be obtained at an ambient temperature. The least viscosity is reported for DES/NADES in the literature [89]. The temperature evolution of viscosity was studied using the VFT model. The coefficients are reported in Table 1. The T_0 VFT-parameter is related to the glass transition temperature [90]. The reported low values (in agreement with the low viscous character of these fluids) indicate a wide liquid window range for these fluids. This indicates their industrial applicability. The fragility parameters D_f (Fig. 4) indicate that the fluids are not highly fragile though the fluids exhibit intermolecular hydrogen bonding (*i.e.*, absence of ionic interactions as in Type III DESs). Large D_f values were recorded for CIT-NADES, indicating that the fluid was strong. Moreover, the HBD effect on fragility follows the order LIN < CILLOL < GER (for most of the NADES systems with the exception of CILLAL). Therefore, strong NADES systems such as CIT:GER are obtained.

The reported experimental properties allowed the characterization of the considered NADES system. Nevertheless, it is important to develop predictive models which allow the study of relevant properties of the involved HBAs/HBDs systems. For this purpose, predictive mathematical methods were studied (to determine the density and viscosity) using ML methods. The methods have been used previously to analyze the properties of DESs and determine their applications [91,92]. The ML methods have not been used to study type V NADESs. Different ML methods were used to determine the density and viscosity data for training. The technique led to the lower *RMSE* being selected: 5/2 GPR and trilayered NN were used to study the density and viscosity, respectively. Excellent correlative abilities were observed (Fig. 5). The developed models were used for predictive purposes (validation sets). Excellent predictions were obtained, and outliers could not predict the properties of the different types of considered monoterpenoid-NADES in the studied temperature range.

3.2. Protein docking, membrane interaction, and hydrophobicity

A simplified model was used to analyze and quantify the biological effects of chemicals and understand their toxicity. The studies were conducted following two primary processes: (i) chemical transportation across cell membranes into cells and (ii) chemical binding with target receptor proteins. Although this approach does not consider the metabolic effects of chemicals, it has been proved to be suitable for describing the toxicity of complex chemicals [93]. The possible biological effects of the considered NADES system were analyzed following three approaches: (i) docking of a target protein was studied, (ii) the octanol–water partition coefficients were determined, and (iii) the interaction with model lipid bilayers, used as a model of penetration through cell membranes, was studied.

The docking results are reported in Fig. 6 and Table S5 (Supplementary Information). Results presented in Fig. 6a indicate the affinity of

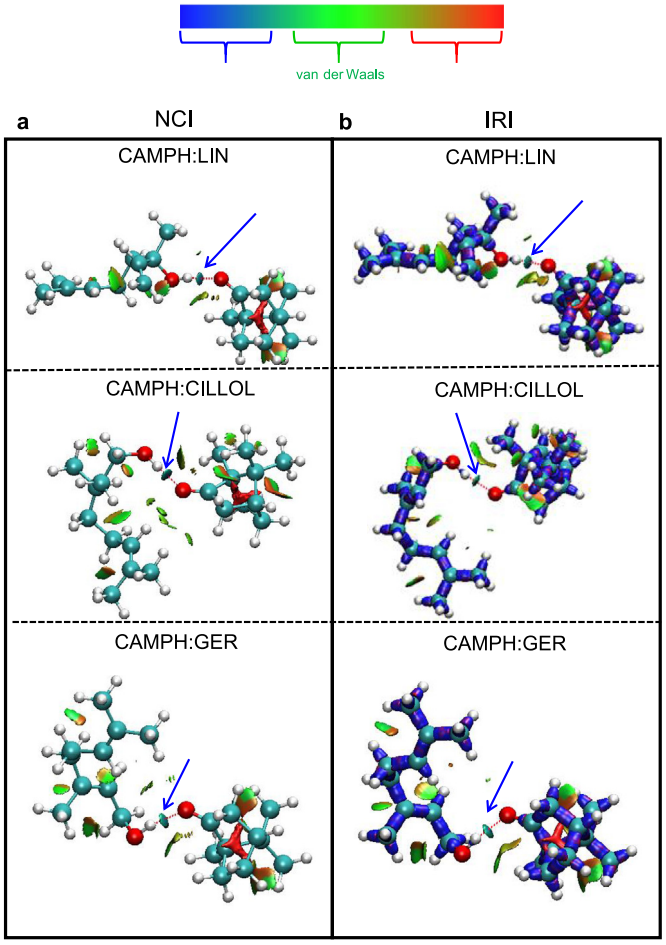

Fig. 10. (a) NCI and (b) IRI analysis of the CAMPH-based clusters using the DFT technique. The blue arrows indicate spots corresponding to intermolecular hydrogen bonding.

Table 3
IR frequencies for the reported vibrations calculated for isolated molecules and HBA:HBD 1:1 cluster. Values are obtained from DFT calculations. Values for the clusters are in bold and values for the corresponding isolated monomers are parenthesized.

Cluster	ν_{st}(O–H @HBD)/cm^{-1}	Shift ν_{st}(O–H @HBD)/cm^{-1}	ν_{st}(C =O @HBA)/cm^{-1}	Shift ν_{st}(O–H @HBD)/cm^{-1}
CAMPH:LIN	**3649.45** (3807.45)	157.77	**1773.68** (1803.78)	30.10
CAMPH:CILLOL	**3666.80** (3823.22)	156.42	**1771.94** (1803.78)	31.84
CAMPH:GER	**3666.20** (3817.85)	151.65	**1773.09** (1803.78)	30.69
CN:LIN	**3633.95** (3807.45)	173.50	— (–)	–
CN:CILLOL	**3681.92** (3823.22)	141.30	— (–)	–
CN:GER	**3672.70** (3817.85)	145.15	— (–)	–
CAR:LIN	**3663.13** (3807.45)	144.32	**1703.58** (1728.63)	25.05
CAR:CILLOL	**3679.33** (3823.22)	143.89	**1702.42** (1728.63)	26.21
CAR:GER	**3647.45** (3817.85)	170.40	**1700.11** (1728.63)	28.52
CILLAL:LIN	**3638.97** (3807.45)	168.48	**1765.88** (1795.56)	29.68
CILLAL:CILLOL	**3656.19** (3823.22)	167.03	**1763.02** (1795.56)	32.54
CILLAL:GER	**3697.43** (3817.85)	120.42	**1771.97** (1795.56)	23.59
CIT:LIN	**3627.55** (3807.45)	179.90	**1756.76** (1788.28)	31.52
CIT:CILLOL	**3612.77** (3823.22)	210.45	**1715.00** (1788.28)	73.28
CIT:GER	**3622.93** (3817.85)	194.92	**1754.63** (1788.28)	33.65

all the considered NADES systems toward the hydrophobic subdomain IIA in the HSE protein (affinities in the −7.0 to −8.5 kcal mol^{-1} range). The docking process of the selected NADES in HAS is characterized by a large number of hydrophobic interactions. The residues form hydrogen bonds, resulting in the efficient packing of NADES in the available protein pocket (Fig. 6b–d). A minor disruption in the HAS structure is observed as the binding of the NADES system in the HBA site can be attributed to hydrophobic interactions. The affinities recorded in this case were lower than the affinities recorded for other chemicals present in different target proteins. Thus, it can be inferred that the considered NADES systems are not highly toxic [93]. The hydrophobic (lipophilic) character of the considered NADESs was quantified through the calculated log(K_{OW}) values (Fig. 7). The reported log(K_{OW}) value confirms the hydrophobic nature of the considered NADES systems. The values were in the range of 6.5–8.0. LID functioned as HBD, and the CILLAL/CIT system at HBAs helped increase the hydrophobicity. Although the HBDs in the considered NADESs contain OH groups, which impart hydrophilicity, these groups are hydrogen bonded to O sites in HBAs, resulting in the formation of NADESs (*i.e.*, the hydrophilic region is placed in the inner region of the HBA–HBD dimmer). This results in the generation of large hydrophobic regions that remain exposed and impart the hydrophobic character to the considered NADESs.

The behavior of the NADES systems as a model lipid bilayer composed of POPC lipids was also studied, and the results are reported in Fig. 8. The results reveal the bilayer permeability (P) and free energy profiles (ΔG). The reported results indicate moderate permeability of the considered NADES (Fig. 8a). The maximum permeability values were recorded for CILLAL/CIT-containing NADES systems. These systems were characterized by the maximum K_{OW} values. A linear correlation was observed between the K_{OW} and p-values (Fig. S3; Supplementary Information). The more hydrophobic NADESs were able to cross the lipid bilayer more easily than the less hydrophobic NADESs. The ΔG profiles reflect the penetration ability of the systems across the lipid membrane (Fig. 8b–f). All the considered NADES systems exhibited similar behavior. This indicated that the systems could cross the bilayer that was stabilized at the center of the membrane. The property is reflected by the lipophilic nature of the considered NADES systems. There is a region between 15 and 25 Å, which can be potentially considered a penetration barrier. Under these conditions, the value of ΔG is low (in absolute value). The process of crossing results in stabilization. This region is present in the vicinity of the polar head groups of the lipids. It is difficult to cross the barrier when hydrophobic fluids are considered. Therefore, the process of crossing the lipid should proceed through the barrier formed by the polar heads. This may constitute the rate-limiting step of the process of crossing the cell membranes. Hence, the hydrophobic nature of the considered NADESs results in the stabilization of the constituent molecules present at the center of the cell membranes and the hydrophobic pockets of target proteins. These are the primary biological effects exerted by these NADES systems. Nevertheless, the permeability values, octanol–water partition coefficients, and protein docking affinities are not significantly high. Thus, bioaccumulation might not occur, and minor disruptions in the structures of the proteins or cell membrane can be observed.

3.3. DFT with minimal cluster approach

Efficient characterization of the physicochemical and biological properties of the considered NADES system at the nanoscopic level requires a deep analysis of the intermolecular interactions and structure of the fluid systems. Particular attention should be paid to the HBA:HBD hydrogen bonding property which determines the primary properties of the NADES systems. In the first stage, the hydrogen bonding property was analyzed using the DFT technique considering a minimal cluster approach. HBA:HBD dimers were used as models. The structure of all the considered HBA:HBD pairs were optimized, and these optimized geometries were used for the calculation of the relevant geometrical, energetic, and electronic properties (Fig. S2; Supplementary Information).

The electronic properties of the HBA:HBD pairs resembling NADESs depend on the properties of the components (HBA/HBD) and the changes occurring in the HBA–HBD hydrogen bonds. The details of the calculated frontier orbitals (HOMO and LUMO) of the isolated constituents of the NADES system (*i.e.*, before the NADES systems were formed) are reported in Fig. 9. The corresponding energy gaps have also been presented. The primary characteristics inferred from the location of the frontier orbitals are reported in Fig. S4 (Supplementary Information). The orbitals are not located in the vicinity of the donor (hydroxyl groups) or acceptor (O atoms) molecular sites. The HOMO of the system generated following the formation of the HBA–HBD pairs (Fig. 9) was similar to the HOMOs of the

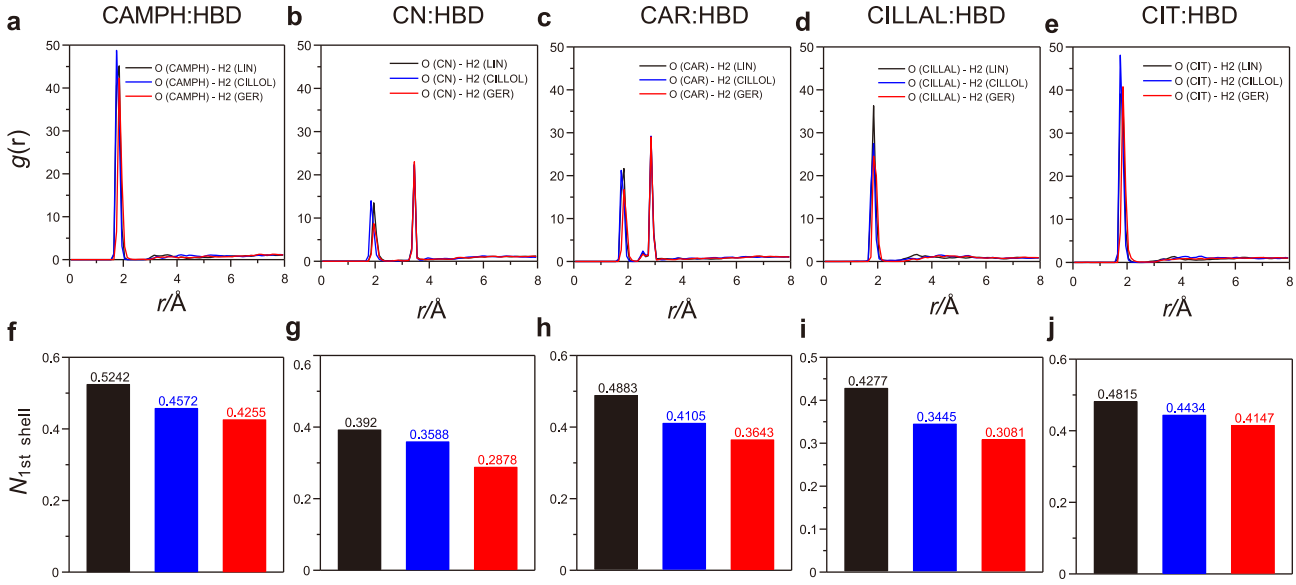

Fig. 11. (a–e) Site–site radial distribution functions, $g(r)$, for the reported atomic pairs (atoms labels presented in Fig. 1) and (f-j) the corresponding integrals of the first solvation shell, $N_{1st\ shell}$, for the considered NADES. Results were obtained using the molecular dynamic simulation technique at 303 K and 1 bar. The first shell was defined with respect to the first minima of the corresponding radial distribution functions.

isolated HBDs. In contrast, the LUMO of the dimers was located in the HBA unit. The HOMO–LUMO energy gaps recorded for isolated HBAs and HBDs (Fig. S4c; Supplementary Information) are in the range of 2.9–5.5 eV. The maximum value was recorded for CN among the HBAs and CILLOL among the HBDs. The maximum gap was recorded for the CN:CILLOL combinations for the HBA–HBD pairs. This could be attributed to the maximum values of the isolated components. For the remaining pairs, the values resemble those of the isolated components (Fig. 9a). This indicates that the primary electronic properties of the HBA–HBD pairs resemble those of the individual components of the pairs.

The electrostatic potentials of the isolated HBAs and HBDs confirm the charge concentration in the acceptor (O atoms) and donor (OH sites) sites, respectively. Analysis of the COSMO σ-profiles results in the development of the well-defined hydrogen bonding acceptor regions in HBAs and donor and acceptor regions in HBDs (Fig. S5a; Supplementary Information). This can be attributed to the combining of the corresponding HBA–HBD pairs. The formation of the HBA–HBD pairs

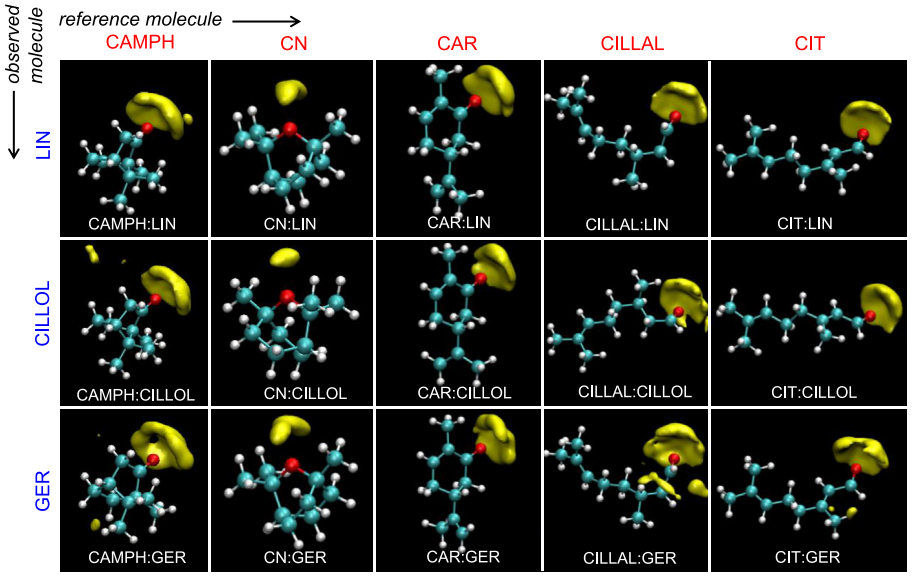

Fig. 12. SDFs used to analyze the considered NADES systems. Results obtained using the molecular dynamics simulation method at 303 K and 1 bar. Values are reported with respect to the HBA (reference molecule), showing the distribution of the corresponding HBDs (observed molecule).

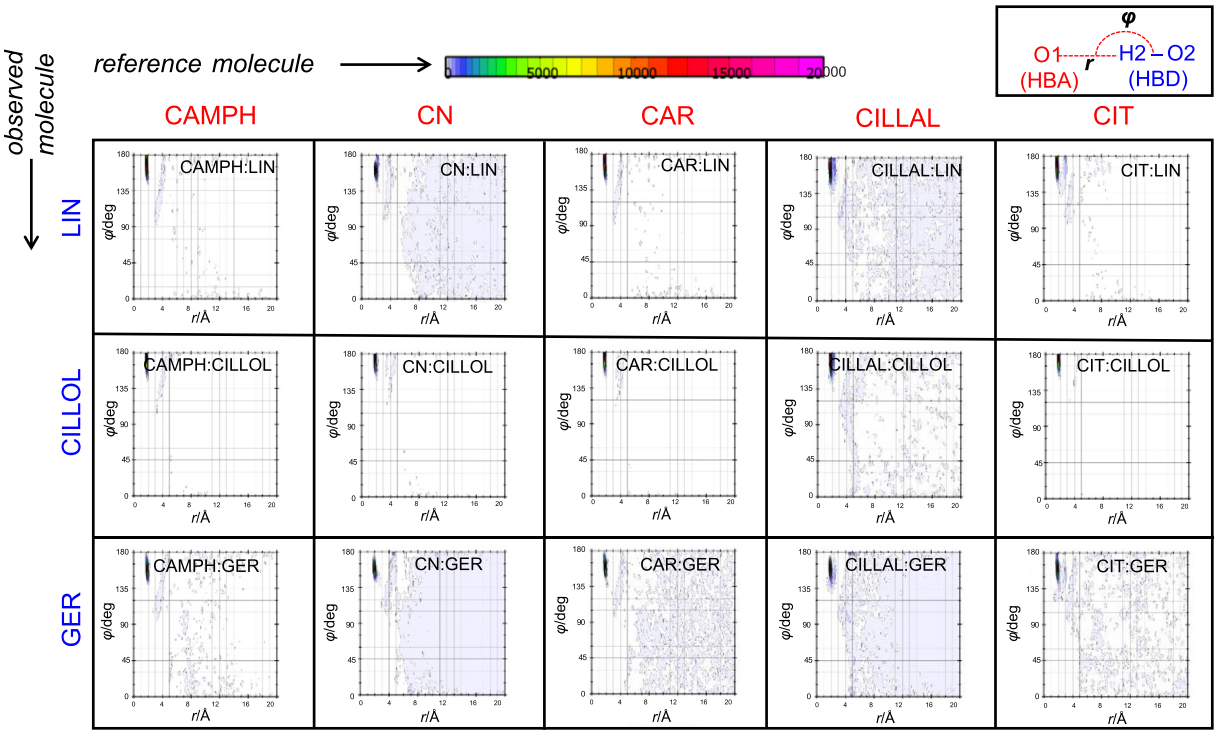

Fig. 13. CDFs for the reported distance, *r*, and angle, *φ*. Functions used for the considered NADES systems to obtain results using the molecular dynamics simulation method at 303 K and 1 bar. Atom labeling as in Fig. 1.

(Fig. S5b; Supplementary Information) results in the generation of a region of charge concentration in the vicinity of the developed hydrogen bonds. The hydrogen bonding ability vanishes while the acceptor properties are maintained. It is noteworthy that beyond the hydrogen bonding region in the HBA–HBD pairs, a large non-polar region is generated, which justifies the hydrophobic nature of these fluids, as indicated in the previous sections.

The development of the HBA–HBD hydrogen bonds following pair formation is confirmed and quantified through the ΔE values (Table 2). The ΔE values range from −16.0 (CILLAL:GER) to −23.1 (CIT:GER) kJ mol^{-1}, confirming the strength of the developed hydrogen bonds. The nature of the developed hydrogen bonds was first analyzed using the QTAIM framework. All the HBA–HBD pairs were characterized by the presence of a bond path joining the donor (OH) and acceptor (O) sites in which a BCP formation is inferred. The properties are reported in Table 2. According to the Popelier criteria [94], hydrogen bonds result in the formation of BCPs. The ρ_e and $\nabla^2\rho_e$ values are in the ranges of 0.002–0.04 a.u. and 0.020–0.139 a.u., respectively. Higher values correspond to stronger H-bonding properties. The average ρ and $\nabla^2\rho$ values were determined from fifteen studied NADES systems, and the values were recorded to be 0.023 (standard deviation: 0.0016) and 0.0859 (standard deviation: 0.0050) a.u. The formation of moderately strong hydrogen bonds is indicated by the ΔE values. There are minor differences in the ρ_e and $\nabla^2\rho_e$ values recorded for the considered NADESs. The results suggest that the lower the ρ_e and $\nabla^2\rho_e$ values, the weaker the hydrogen bonds. A linear relationship was observed between the QTAIM properties (for the BCPs) and ΔE (Fig. S6a–b; Supplementary Information). The HBA–HBD hydrogen bonds were also analyzed based on CVB. The average value recorded for the considered pairs is 0.0213 (standard deviation: 0.0071). The value indicates moderately strong interactions. A roughly linear relationship is observed between the CVB and ΔE values recorded for the considered HBA:HBD pairs. The lower the CVB, the weaker the hydrogen bond (Fig. S6c; Supplementary Information) (see Table 3).

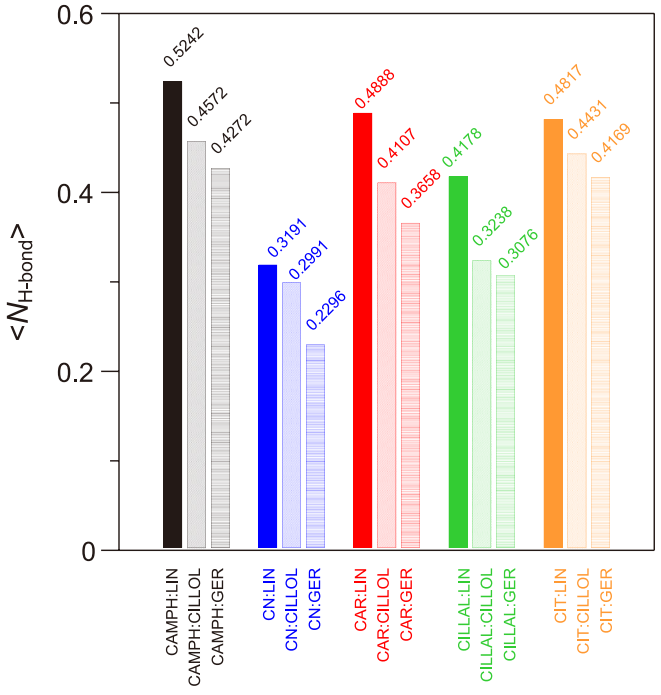

Fig. 14. Average number of HBA–HBD hydrogen bonds per HBA molecule, $<N_{H-bond}>$, present in the considered NADES systems. Results obtained by conducting molecular dynamics simulations at 303 K and 1 bar. All hydrogen bonds correspond to O1(HBA)–O2(HBD) interactions (Fig. 1).

The hydrogen bond distances reported in Table 2 are in the range of 1.92–2.01 Å for the considered pairs. The values indicate moderately strong interactions. The NCI and IRI analysis of the HBA–HBD pairs (Fig. 10) confirms the development of the hydrogen bonds in the O(HBA) to OH(HBD) regions. The results were arrived at by analyzing the reported interaction spots present along the interatomic lines. Additional spots in the HBA–HBD interacting regions corresponding to van der Waals-like interactions and contributing to the stabilization of the interacting pairs were observed for NCI and IRI. The spots appeared in the region beyond the localized hydrogen bonding region. Red-shifted OH(HBD) and CO(HBA) stretching frequencies were observed in the predicted IR spectra of the interacting pairs. This reflected a weakening of the corresponding bonds in the donor and acceptor sites. A linear relationship between the hydrogen bond strength and the red-shifting property, especially for the OH sites in HBDs, was observed (Fig. S7; Supplementary Information).

3.4. MD simulations

The nanoscopic analysis of the properties of the liquid phases corresponding to the considered NADESs was carried out using classical MD simulation techniques. The radial distribution functions (RDFs) for hydrogen bond donor and acceptor sites are reported in Fig. 11. An intense RDF peak at 1.95 Å was observed for all the NADES systems under consideration. The results agree with the hydrogen bonding distance obtained using the DFT technique. The results are presented in Table 2. Therefore, the strength of the HBA–HBD interactions in the bulk liquid

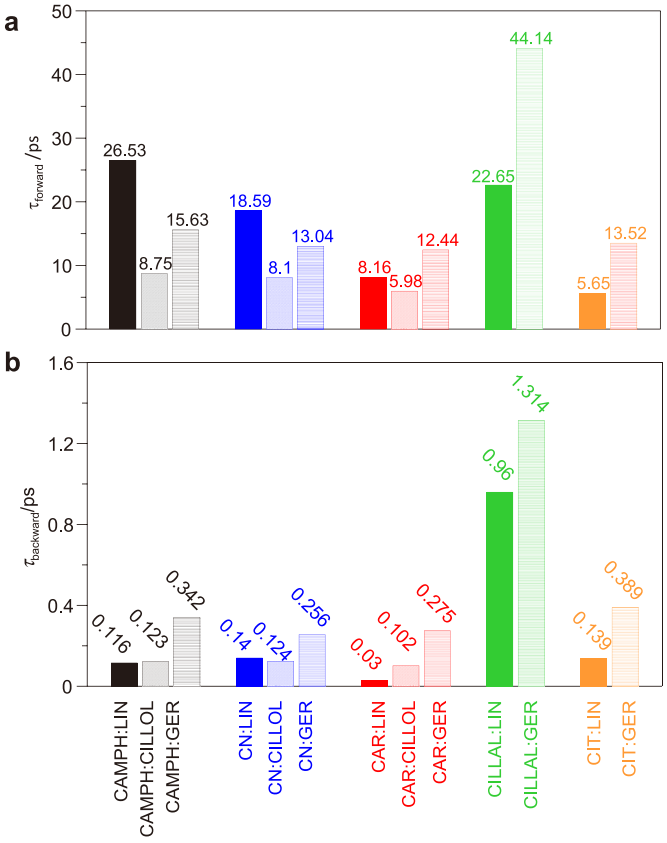

Fig. 15. Dynamics of the hydrogen bonds in the reported atomic pairs corresponding to the considered NADES systems. Results obtained by conducting molecular dynamics simulations at 303 K and 1 bar. All hydrogen bonds correspond to O1(HBA) – O2(HBD) interactions (Fig. 1). Results in panel (a) show time, τ, for the forward process (*i.e.*, hydrogen bonds lifetime), and those in panel (b) present the time corresponding to the backward process (*i.e.*, the formation of hydrogen bonds post breaking).

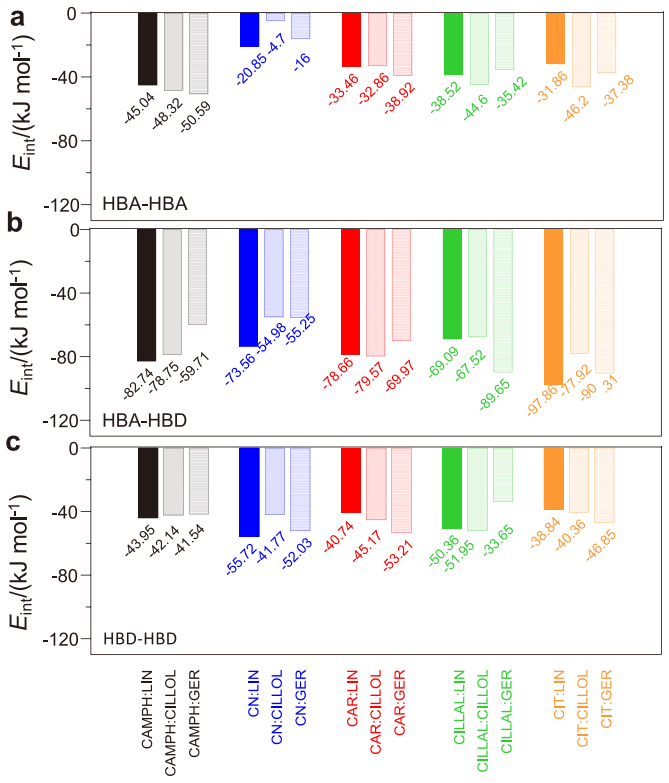

Fig. 16. Intermolecular interaction energy, E_{int}, recorded for the reported molecular pairs present in the considered NADES systems. Results obtained by conducting molecular dynamics simulations at 303 K and 1 bar.

phase is equal to that inferred from the HBA–HBD interactions in the dimers. In the case of CN-and CAR-containing NADES systems (Fig. 11b and c), a second RDF peak appears at 3.5 and 2.9 Å, respectively. This is accompanied by the first RDF peak, and the intensity of this peak is less than the intensity of the peaks recorded for the other NADES systems. This indicates that the molecules are organized when in direct contact with hydrogen bonds. The integration of the first peak in RDFs is reported in Fig. 11f–j, *i.e.*, the number of OH(HBDs) around a central O(HBD) has been presented. This helps the formation of hydrogen bonds. These results indicate that the number of HBDs in the first solvation shell decrease, following in the order LIN > CILLOL > GER for all the considered HBAs. The distribution of HBDs around the HBAs is shown in Fig. 12. The distribution is recorded based on the spatial distribution functions (SDFs). SDFs show highly localized spots around the O atoms, *i.e.*, around the hydrogen bond acceptor sites in the cases of all the considered HBAs. For the case of the CN – based NADES, the extension of these spots is less intense. This is in agreement with the RDFs reported in Fig. 11. The generation of a small amount of certain steric can be attributed to the location of the acceptor site inside the CN molecule. The effect of the type of HBD under consideration on the SDFs is almost negligible. In all the cases, the HBDs were located in the vicinity of the O(HBD) sites. The reported SDFs reveal that the HBDs were concentrated around the O(HBA) sites, resulting in the generation of a large number of non-interacting molecules. This results in the generation of large hydrophobic domains, the origin of which can be attributed to the entry of the HBAs and the HBDs into the liquid phases of the NADES systems.

The nature of the developed hydrogen bonds was confirmed by analyzing the combined distribution functions (CDFs). These functions reveal the separation between and orientation of the donor and acceptor sites (Fig. 13). The CDF values corresponding to the considered NADES systems reveal the presence of the major spots at 1.95 Å and 160°. This confirms the formation of hydrogen bonds. The minor differences observed were attributed to the types of the HBA or HBD systems under consideration. The extension of the hydrogen bonding property can be quantified by considering the number of hydrogen bonds per molecule (Fig. 14). The trend LIN > CILLOL > GER was confirmed, and it was observed that a small number of hydrogen bonds were present in CN-containing NADES. This extension of the hydrogen bonds and the presence of the highly localized interactions in the studied NADES systems should justify the low viscous character of these fluids. In other words, it was inferred that the development of the hydrogen bonds allows the formation of the NADES system (*i.e.*, the melting point decreases). As the bonds are developed in localized spots (dimers connected through hydrophobic domains), low viscosity is generated.

Besides the structure of the fluids characterized by the presence of hydrogen bonding and hydrophobic domains, the dynamic properties of the considered NADES are analyzed based on reactive flux analysis [95]. The hydrogen bonding lifetime (forward process) and the time required for interaction reformation following the breakage of the bonds (backward process) were studied (Fig. 15). The results indicate the formation of short-lived hydrogen bonds. This agrees well with the interaction energies reported in Table 2. Rapid reformation of the interactions, *i.e.*, highly dynamic hydrogen bonding networks, was also observed. The general trends in the changes in the lifetimes do not depend on the type of HBA/HBD systems considered. The times were in the range of 6–44 ps for the considered NADES, whereas the reforming time was always lower than 1.3 ps. This rapid reforming process observed for the considered

Table 4
Domain analysis from MD simulations of NADES (HBA: HBD 1:1) at 303 K and 1 bar. Domain volume, *D-vol*, domain area, *D-surf*, and isoperimetric index, Q^{peri}, are reported.

HBA	HBD	HBD domain				HBA domain			
		Domain count	*D-vol*/Å^3	*D-surf*/Å^2	Q^{peri}	Domain count	*D-vol*/Å^3	*D-surf*/Å^2	Q^{peri}
CAMPH	LIN	1	165423.97	75156.31	0.0849	1	148426.27	75420.16	0.0762
	CILLOL	1	168632.76	75602.40	0.0862	1	145507.79	75451.20	0.0744
	GER	1	166587.90	74874.27	0.0864	1	147612.02	74836.73	0.0765
CN	LIN	1	164382.32	73971.30	0.0868	1	150049.67	73971.30	0.0793
	CILLOL	1	165560.57	70982.36	0.0931	1	148871.42	70982.36	0.0837
	GER	1	164567.44	71595.51	0.0911	2	58539.777	28059.79	0.4678
CAR	LIN	1	165438.21	75637.61	0.0844	1	148235.46	75409.77	0.0782
	CILLOL	1	168092.72	73937.16	0.0889	1	146265.98	73900.22	0.0777
	GER	1	162847.24	73846.5	0.0847	1	149458.32	74667.54	0.0777
CILLAL	LIN	1	158843.70	77981.65	0.0775	1	155588.29	77981.65	0.0759
	CILLOL	1	157969.40	71131.86	0.0885	1	156462.59	71131.86	0.0877
	GER	1	154673.43	76527.98	0.0776	1	159758.56	76527.98	0.0802
CIT	LIN	1	160229.78	78746.14	0.0771	1	154202.21	78746.14	0.0742
	CILLOL	1	275017.74	103112.83	0.0883	1	252947.57	101722.81	0.0891
	GER	1	158635.19	77932.98	0.0775	1	155796.80	77932.98	0.0761

fluids lies in one extreme of the interaction strength. The formation of moderately strong hydrogen bonds is also observed. Highly localized interactions (polar spots surrounded by apolar (hydrophobic) domains) were also recorded. The strength of the interactions in the liquid phases is presented in Fig. 16. It is noteworthy that homo-associations (HBA–HBA) can also be formed through dipolar interactions. HBD–HBD pairs can also be formed by exploiting dipolar and hydrogen bonding interactions. The results presented in Fig. 16 indicate the presence of strong and extensive HBA–HBD. The strength of these interactions is higher than the strength of the interactions observed for the cases of HBA–HBA or HBD–HBD. In the case of the HBA–HBA interactions, significantly low interaction energy values are recorded for the CN-based NADES systems, whereas for the remaining fluids, it was observed that the properties of the HBA–HBA systems were comparable to the properties of the HBD–HBD systems. The interaction energies for the HBA–HBD system were analyzed, and the results indicate the formation of moderately strong hydrogen bonds. The strength tends to decrease in the order LIN > CILLOL > GER. However, this is not true for all systems. Hydrogen bonds were formed in all the cases. The analysis of large range aggregation was carried out using the domain analysis method [96]. The Voronoi-based method was used for the studies, as reported in Table 4. Results obtained using the domain analysis method indicate that the domains corresponding to HBA and HBD extend throughout the fluid, *i.e.*, large and interconnected domains with non-spherical shapes (close to zero isoperimetric indices) are formed. The formation of these domains can be attributed to the generation of non-polar hydrophobic sites in the HBA/HBD molecules.

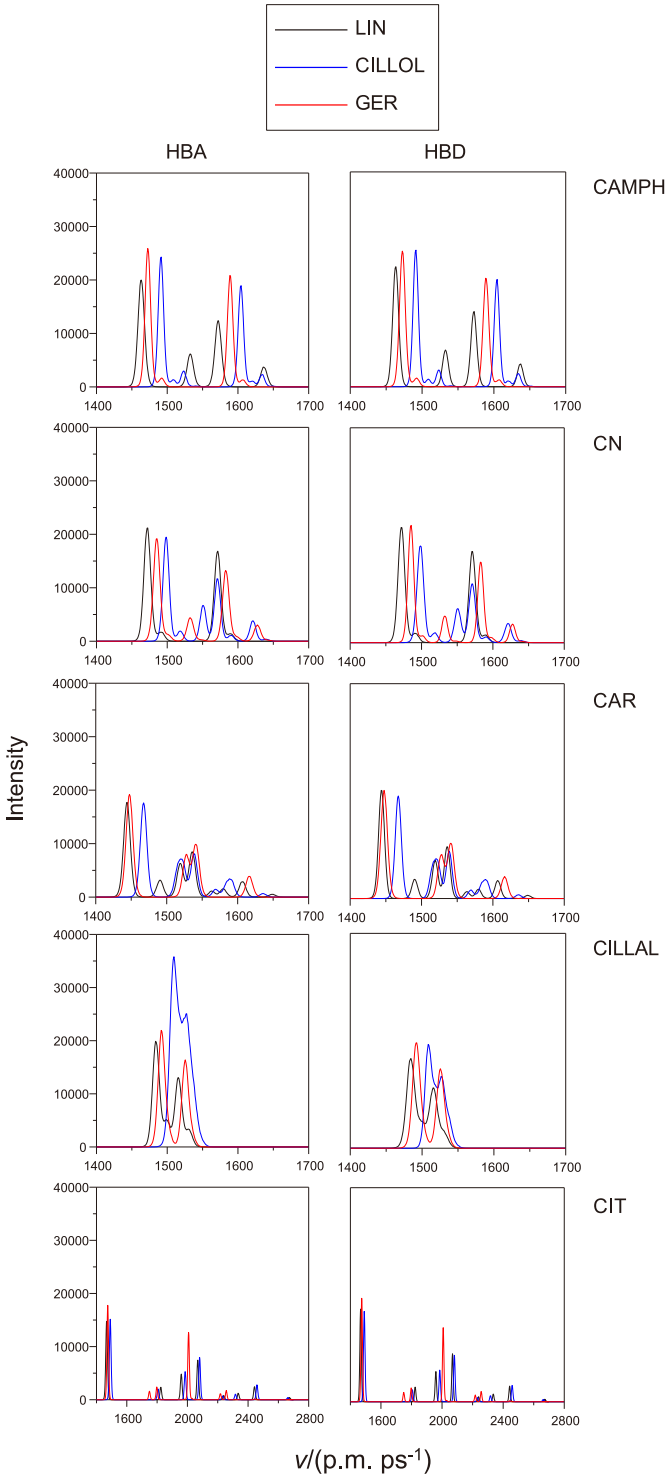

Fig. 17. Velocity distribution functions for the considered NADES systems. Results obtained using by conducting molecular dynamics simulations at 303 K and 1 bar. The left and right columns indicate values for HBA and HBD, respectively.

The molecular dynamics of the involved HBA and HBD molecules were quantified, and the results are presented in Fig. 17. A complex dynamics is inferred for all the cases. Several peaks corresponding to molecules were recorded under conditions of different environments, and the velocities were found to vary in the range of 1450–1650 p.m. ps^{-1}. Each of the NADES velocity distribution profiles is comparable to those of the involved HBA and HBD systems. In other words, highly correlated molecular movements attributable to the generation of hydrogen bonds were recorded. The HBD effect was recorded, and it was inferred that the velocity corresponding to the LIN system was low and that recorded for the GER system was high. This reflects the extension of the hydrogen bonds (Fig. 14). The effect of HBA is almost negligible, and the maximum differences were recorded for the CIT-containing NADES systems. Therefore, the NADES systems are characterized by moderately strong hydrogen bonds that are highly localized around O(HBA) atoms. Dynamic interactions and fast molecular mobility result in the formation of less dense and less viscous hydrophobic fluids.

4. Conclusions

The properties of less viscous monoterpenoid-based type V NADES systems were analyzed using a combination of experimental and modeling methods. The reported results revealed that the hydrophobic fluids with low density and significantly low viscosity and characterized by suitable physicochemical properties could be used in various technological fields. Analysis of the ecotoxicological properties revealed that the hydrophobic nature of these fluids results in the generation of moderate octanol-water partition coefficients. This indicates that the systems can penetrate the cellular membranes and relevant sites of target proteins without causing significant disruptions in the biological environments. These eutectics are characterized by the presence of moderately strong and highly localized hydrogen bonds. These bonds are present around the acceptor sites in the monoterpenoids, and the presence of these bonds results in the formation of highly dynamic nanostructures with localized polar spots. The hydrogen bonds are developed amidst large hydrophobic environments. The results reveal that heterogeneous fluids are developed at the nanoscopic level. The structure and properties of the proposed fluids resemble those of the deep eutectics. Hydrophobic features were also observed, and the systems were characterized by low viscosity. This results in the generation of a suitable platform for developing hydrophobic systems that are cost-effective, nontoxic, and natural.

Declaration of competing interests

The authors declare that they have no known competing financial

interests or personal relationships that could have appeared to influence the work reported in this paper.

Acknowledgments

This work was funded by the Junta de Castilla y Leon (Spain, project NANOCOMP-BU058P20) and the Ministerio de Ciencia, Innovación y Universidades (Spain, project RTI2018–101987-B-I00). We also acknowledge SCAYLE (Supercomputación Castilla y León, Spain) for providing supercomputing facilities. The statements made herein are solely the responsibility of the authors.

Appendix A. Supplementary data

Supplementary data to this article can be found online at https://doi.org/10.1016/j.gce.2022.05.005.

References

[1] A.P. Abbott, G. Capper, D.L. Davies, H.L. Munro, R.K. Rasheed, V. Tambyrajah, Preparation of novel, moisture-stable, Lewis-acidic ionic liquids containing quaternary ammonium salts with functional side chains, Chem. Commun. 19 (2001) 2010–2011.
[2] A. Paiva, R. Craveiro, I. Aroso, M. Martins, R.L. Reis, A.R.C. Duarte, Natural deep eutectic solvents–solvents for the 21st century, ACS Sustainable Chem. Eng. 2 (2014) 1063–1071.
[3] X. Ge, C. Gu, X. Wang, J. Tu, Deep eutectic solvents (DESs)-derived advanced functional materials for energy and environmental applications: challenges, opportunities, and future vision, J. Mater. Chem. 5 (2017) 8209–8229.
[4] A.P. Abbott, J.C. Barron, K.S. Ryder, D. Wilson, Eutectic-based ionic liquids with metal-containing anions and cations, Chem. Eur. J. 13 (2007) 6495–6501.
[5] S. Dutta, K. Nath, Prospect of ionic liquids and deep eutectic solvents as new generation draw solution in forward osmosis process, J. Water Proc. Eng. 21 (2018) 163–176.
[6] W. Jiang, H. Jia, H. Li, L. Zhu, R. Tao, W. Zhu, H. Li, S. Dai, Boric acid-based ternary deep eutectic solvent for extraction and oxidative desulfurization of diesel fuel, Green Chem. 21 (2019) 3074–3080.
[7] L.L. Sze, S. Pandey, S. Ravula, S. Pandey, H. Zhao, G.A. Baker, S.N. Baker, Ternary deep eutectic solvents tasked for carbon dioxide capture, ACS Sustainable Chem. Eng. 2 (2014) 2117–2123.
[8] R. Gupta, J. Gamare, M. Sahu, K. Pandey, S.K. Gupta, Electrochemical and thermodynamic insights on actinide type (IV) deep eutectic solvent, J. Mol. Liq. 329 (2021) 115550.
[9] L. Xu, Y. Luo, H. Liu, J. Yin, H. Li, W. Jiang, W. Zhu, H. Li, H. Ji, Extractive desulfurization of diesel fuel by amide based type IV deep eutectic solvents, J. Mol. Liq. 338 (2021) 116620.
[10] D.O. Abranches, M.A. Martins, L.P. Silva, N. Schaeffer, S.P. Pinho, J.A. Coutinho, Phenolic hydrogen bond donors in the formation of non-ionic deep eutectic solvents: the quest for type V DES, Chem. Commun. 55 (2019) 10253–10256.
[11] G. García, S. Aparicio, R. Ullah, M. Atilhan, Deep eutectic solvents: physicochemical properties and gas separation applications, Energy Fuel. 29 (2015) 2616–2644.
[12] L.I.N. Tomé, V. Baiao, W. da Silva, M.A. Brett, Deep eutectic solvents for the production and application of new materials, Appl. Mater. Today 10 (2018) 30–50.
[13] Y.H. Choi, J. van Spronsen, Y. Dai, M. Verberne, F. Hollmann, I.W.C.E. Arends, G.J. Witkamp, R. Verpoorte, Are natural deep eutectic solvents the missing link in understanding cellular metabolism and physiology? Plant Phisiol. 156 (2011) 1701–1705.
[14] Y. Dai, J. van Spronsen, G.J. Witkamp, R. Verpoorte, Y.H. Choi, Natural deep eutectic solvents as new potential media for green technology, Anal. Chim. Acta 766 (2013) 61–68.
[15] Y. Liu, J.B. Friesen, J.B. McAlpine, D.C. Lankin, S.N. Chen, G.F. Pauli, Natural deep eutectic solvents: properties, applications, and perspectives, J. Nat. Prod. 81 (2018) 679–690.
[16] M.A. Fernández, J. Boiteux, M. Espino, F.J. Gomez, M.F. Silva, Natural deep eutectic solvents-mediated extractions: the way forward for sustainable analytical developments, Anal. Chim. Acta 1038 (2018) 1–10.
[17] T. Zhekenov, N. Toksanbayev, Z. Kazakbayeva, D. Shah, F.S. Mjalli, Formation of type III deep eutectic solvents and effect of water on their intermolecular interactions, Fluid Phase Equil. 441 (2017) 43–48.
[18] O.S. Hammond, D.T. Bowron, K.J. Edler, The effect of water upon deep eutectic solvent nanostructure: an unusual transition from ionic mixture to aqueous solution, Angew. Chem. Int. Ed. 129 (2017) 9914–9917.
[19] C. Florindo, L.C. Branco, I.M. Marrucho, Quest for green-solvent design: from hydrophilic to hydrophobic (deep) eutectic solvents, ChemSusChem 2 (2019) 1549–1559.
[20] C. Fan, T. Sebbah, X. Cao, Terpenoid-capric acid based natural deep eutectic solvent: insight into the nature of low viscosity, Clean. Eng. Technol. 3 (2021) 100116.
[21] B.B. Hansen, S. Spittle, B. Chen, D. Poe, Y. Zhang, J.M. Klein, A. Horton, L. Adhikari, T. Zelovich, B.W. Doherty, B. Gurkan, E.J. Maginn, A. Ragauskas, M. Dadmun, T.A. Zawodzinski, G.A. Baker, M.E. Tuckerman, R.F. Savinell, J.R. Sangoro, Deep eutectic solvents: a review of fundamentals and applications, Chem. Rev. 121 (2021) 1232–1285.
[22] J. Plotka-Wasylka, M. de la Guardia, V. Andruch, M. Vilova, Deep eutectic solvents vs ionic liquids: similarities and differences, Microchem. J. 159 (2020) 105539.
[23] N. Fanjul-Mosteirín, V. del Amo, Organocatalytic transformations in deep eutectic solvents: green methodologies made greener, Tetrahedron 84 (2021) 131967.
[24] E. Silva, F. Oliveira, J.M. Silva, R.L. Reis, A.R.C. Duarte, Untangling the bioactive properties of therapeutic deep eutectic solvents based on natural terpenes, Curr. Chem. Biol. 1 (2021) 100003.
[25] X. Chen, F. Wang, S. Liu, Q. Yu, W. Wang, Y. Zhang, Z. Wang, Z. Yuan, Improvement of conversion efficiency from D-glucose to D-allulose by whole-cell catalysts with deep eutectic solvents, ACS Food Sci. Technol. 7 (2021) 1323–1332.
[26] A. Kityk, M. Hnatko, V. Pavlik, M. Boca, Electrochemical surface treatment of manganese stainless steel using several types of deep eutectic solvents, Mater. Res. Bull. 141 (2021) 111348.
[27] T. Aissaoui, I.M. AlNashef, U.A. Qureshi, Y. Benguerba, Potential applications of deep eutectic solvents in natural gas sweetening for CO_2 capture, Rev. Chem. Eng. 33 (2017) 523–550.
[28] W. Wang, D.J. Lee, Lignocellulosic biomass pretreatment by deep eutectic solvents on lignin extraction and saccharification enhancement: a review, Bioresour. Technol. 339 (2021) 125587.
[29] N. Schaeffer, D.O. Abranches, L.P. Silva, M.A.R. Martins, P.J. Carvalho, O. Russina, A.T. Triolo, L. Paccou, Y. Guinet, A. Hedoux, J.A.P. Coutinho, Non-ideality in thymol + menthol type V deep eutectic solvents, ACS Sustainable Chem. Eng. 9 (2021) 2203–2221.
[30] M.A.R. Martins, S.P. Pinho, J.A.P. Cotinho, Insights into the nature of eutectic and deep eutectic mixtures, J. Solut. Chem. 48 (2019) 962–982.
[31] G. Tarelli, E.N. Zerba, R.A. Alzogaray, Toxicity to vapor exposure and topical application of essential oils and monoterpenes on *Musca domestica* (diptera: muscidae), J. Econ. Entomol. 102 (2009) 1383–1388.
[32] E. Kahraman, N. Nesetoglu, S. Güngur, D.S. Umal, Y. Ozsoy, The combination of nanomicelles with terpenes for enhancement of skin drug delivery, Int. J. Pharm. 551 (2018) 133–140.
[33] A. Koziol, A. Stryjewska, T. Librowski, K. Salat, M. Gawel, A. Moniczewski, S. Lochynski, An overview of the pharmacological properties and potential applications of natural monoterpenes, Mini Rev. Med. Chem. 14 (2018) 1156–1168.
[34] M.M. Abdallah, S. Müller, A. González, P. Gurikov, A.A. Matias, M.R. Bronze, N. Fernandez, Physicochemical characterization and simulation of the solid–liquid equilibrium phase diagram of terpene-based eutectic solvent systems, Molecules 26 (2021) 1801.
[35] M. Zielinska-Blajet, J.F. Kubis, Monoterpenes and their derivatives—recent development in biological and medical applications, Int. J. Mol. Sci. 21 (2020) 7078.
[36] K. Li, Y. Jin, K. Park, H. Kim, J. Lee, *In situ* formation of thymol-based hydrophobic deep eutectic solvents: application to antibiotics analysis in surface water based on liquid-liquid microextraction followed by liquid chromatography, J. Chromatogr. A 1614 (2020) 460730.
[37] C. Fan, Y. Liu, X. Cao, A theoretical study on terpene-based natural deep eutectic solvent: relationship between viscosity and hydrogen-bonding interactions, Global Chall 5 (2021) 2000103.
[38] L.A. Rodrigues, C.V. Pereira, I.C. Leonardo, N. Fernandez, F.B. Gaspar, J.M. Silva, R.L. Reis, A.R.C. Duarte, A. Paiva, A.A. Matias, Terpene-based natural deep eutectic systems as efficient solvents to recover astaxanthin from brown crab shell residues, ACS Sustainable Chem. Eng. 8 (2020) 2246–2259.
[39] C. Velez, O. Acevedo, Simulation of deep eutectic solvents: progress to promises, WIRES Comput. Mol. Sci. (2022) e1598.
[40] D. Tolmachev, N. Lukasheva, R. Ramazanov, V. Nazaychev, N. Borzdum, I. Volgin, M. Andreeva, A. Glova, Melnikova, A. Dobrovsky, S.A. Silber, S. Larin, R. Maglia de Souza, M.C. Costa-Ribeiro, S. Lyulin, M. Karttunen, Computer simulations of deep eutectic solvents: challenges, solutions, and perspectives, Int. J. Mol. Sci. 23 (2022) 645.
[41] Z. Naseem, R.A. Shehzad, A. Ihsan, J. Iqbal, M. Zahid, A. Pervaiz, G. Sarwari, Theoretical investigation of supramolecular hydrogen-bonded choline chloride-based deep eutectic solvents using density functional theory, Chem. Phys. Lett. 769 (2021) 138427.
[42] L.H. Xu, D. Wu, M. Zhong, G.B. Wang, X.Y. Chen, Z.J. Zhang, The construction of a new deep eutectic solvents system based on choline chloride and butanediol: the influence of the hydroxyl position of butanediol on the structure of deep eutectic solvent and supercapacitor performance, J. Power Sources 490 (2021) 229365.
[43] K. Kumar, S. Keshri, A.S. Bharti, S. Kumar, S. Mogurampelly, Solubility of gases in choline chloride-based deep eutectic solvents from molecular dynamics simulation, Ind. Eng. Chem. Res. 61 (2022) 4659–4671.
[44] A. Gutierrez, M. Atilhan, S. Aparicio, Theoretical study on deep eutectic solvents as vehicles for the delivery of anesthetics, J. Phys. Chem. B 124 (2020) 1794–1805.
[45] M. Atilhan, S. Aparicio, Molecular dynamics simulations of metal nanoparticles in deep eutectic solvents, J. Phys. Chem. C 122 (2018) 18029–18039.
[46] M. Atilhan, S. Aparicio, Molecular dynamics study on the use of deep eutectic solvents for enhanced oil recovery, J. Petrol. Sci. Eng. 209 (2022) 19953.
[47] V. Alizadeh, F. Malberg, A.A.H. Padua, B. Kirchner, Are there magic compositions in deep eutectic solvents? Effects of composition and water content in choline chloride/ethylene glycol from ab initio molecular dynamics, J. Phys. Chem. B 124 (2020) 7433–7443.
[48] S.B. Pour, J.J. Sardroodi, A.R. Ebrahimzadeh, The study of structure and interactions of glucose-based natural deep eutectic solvents by molecular dynamics simulation, J. Mol. Liq. 334 (2021) 115956.

[49] M. Abdollahzadeh, M. Khosravi, B.H. Masjidi, A.S. Behbahan, A. Bagherzadeh, A. Shahkar, F.T. Shahdost, Estimating the density of deep eutectic solvents applying supervised machine learning techniques, Sci. Rep. 12 (2022) 4954.
[50] D.O. Abranches, J.A.P. Coutinho, Type V deep eutectic solvents: design and applications, Curr. Opin. Green Sus. Chem. 35 (2022) 100612.
[51] A. Kovacs, E.C. Neyts, I. Cornet, M. Wijnants, P. Billen, Modeling the physicochemical properties of natural deep eutectic solvents, ChemSusChem 13 (2020) 3789–3804.
[52] R. Alcalde, G. García, M. Atilhan, S. Aparicio, Thermophysical properties of pure ionic liquids: review of present situation, Ind. Eng. Chem. Res. 54 (2015) 10918–10924.
[53] V.G. Machado, R.I. Stock, C. Reichardt, Pyridinium N-phenolate betaine dyes, Chem. Rev. 114 (2014) 10429–10475.
[54] A. Cherkasov, Inductive QSAR descriptors. distinguishing compounds with antibacterial activity by artificial neural networks, Int. J. Mol. Sci. 6 (2005) 63–86.
[55] S.G. Balasumramani, G.P. Chen, S. Coriani, M. Diedenhofer, M.S. Frank, Y.J. Franzke, F. Furche1, R. Grotjahn, M.E. Harding, C. Hattig, A. Hellweg, B. Helmich-Paris, C. Holzer, U. Huniar, M. Kaupp, A.M. Khah, S.K. Khani, T. Müller, F. Mack, B.D. Nguyen, S.M. Parker, E. Perlt, D. Rappoport, K. Reiter, S. Roy, M. Rückert, G. Schmitz, M. Sierka, E. Tapavicza, D.P. Tew, C. van Wüllen, V.K. Voora, F. Weigend, A. Wodyński, J.M. Yu, TURBOMOLE: modular program suite for *ab initio* quantum-chemical and condensed-matter simulations, J. Chem. Phys. 152 (2020) 184107.
[56] I. Sushko, S. Novotarskyi, R. Körner, A.K. Pandey, M. Rupp, W. Teetz, S. Brandmaier, A. Abdelaziz, V.V. Prokopenko, V.Y. Tanchuk, R. Todeschini, A. Varnek, G. Marcou, P. Ertl, V. Potemkin, M. Grishina, J. Gasteiger, S.C. Baskin, V.A. Palyulin, E.V. Radchenko, W.J. Welsh, V. Kholodovych, D. Chekmarev, A. Cherkasov, J. Aires-de-Sousa, Q.Y. Zhang, A. Bender, F. Nigsch, L. Patiny, A. Williams, V. Tkachenko, I.V. Tetko, Online chemical modeling environment (OCHEM): web platform for data storage, model development and publishing of chemical information, J. Comput. Aided Mol. Des. 25 (2011) 533–554.
[57] F. Neese, The ORCA program system, WIRES Comput. Mol. Sci. 2 (2011) 73–78.
[58] C. Lee, W. Yang, R.G. Parr, Development of the colle-salvetti correlation-energy formula into a functional of the electron density, Phys. Rev. B 37 (1988) 785–789.
[59] A.D. Becke, Density-functional exchange-energy approximation with correct asymptotic behavior, Phys. Rev. A 38 (1988) 3098–3100.
[60] A.D. Becke, Density-functional thermochemistry. III. The role of exact exchange, J. Chem. Phys. 98 (1993) 5648–5652.
[61] S. Grimme, J. Antony, H. Krieg, A consistent and accurate *ab initio* parametrization of density functional dispersion correction (DFT-D) for the 94 elements H-Pu, J. Chem. Phys. 132 (2010) 154104.
[62] M.D. Hanwell, D.E. Curtis, D.C. Lonie, T. Vandermeerch, E. Zurek, G.R. Hutchinson, Avogadro: an advanced semantic chemical editor, visualization, and analysis platform, J. Cheminf. 4 (2012) 17.
[63] S. Simon, M. Duran, J. Dannenberg, How does basis set superposition error change the potential surfaces for hydrogen-bonded dimers? J. Chem. Phys. 105 (1996) 11024.
[64] R.F.W. Bader, Atoms in molecules, Acc. Chem. Res. 18 (1985) 9–15.
[65] Tian Lu, F. Chen, Multiwfn: a multifunctional wavefunction analyzer, J. Comput. Chem. 33 (2012) 580–592.
[66] E.R. Johnson, S. Keinan, P. Mori-Sanchez, J. Contreras-García, A.J. Cohen, W. Yang, Revealing noncovalent interactions, J. Am. Chem. Soc. 132 (2010) 6498–6506.
[67] D.T. Lu, Q. Chen, Interaction region indicator (IRI): a very simple real space function clearly revealing both chemical bonds and weak interactions, Chem. Methods 1 (2021) 231–239.
[68] F. Fuster, B. Silvi, Topological analysis of the electron localization function (ELF) applied to the electrophilic aromatic substitution, Theor. Chem. Acc. 104 (2000) 13–21.
[69] M.M. Trush, I.V. Semenyuta, D. Hodyna, A.D. Ocheretniuk, S.I. Vdovenko, S.P. Rogalsky, L.E. Kalashnikova, V. Blagodatnyi, O.L. Kobzar, L.O. Meterlytsia, Functionalized imidazolium-based ionic liquids: biological activity evaluation, toxicity screening, spectroscopic, and molecular docking studies, Med. Chem. Res. 29 (2020) 2181–2191.
[70] O. Trott, A.J. Olson, AutoDock Vina, Improving the speed and accuracy of docking with a new scoring function, efficient optimization and multithreading, J. Comput. Chem. 31 (2010) 455–461.
[71] M.F. Adasme, K.L. Linnemann, S.N. Bolz, F. Kaiser, S. Salentin, J. Haupt, M. Schroeder, PLIP 2021: expanding the scope of the protein–ligand interaction profiler to DNA and RNA, Nucleic Acids Res. 49 (2021) W530–W534.
[72] BIOVIA COSMOtherm, Dassault systèmes. http://www.3ds.com 2022 (accesed 10 March 2022).
[73] J.A.H. Schwöbel, A. Ebert, K. Bittermann, K.U. Goss, A. Klamt, COSMOperm: mechanistic prediction of passive membrane permeability for neutral compounds and ions and its pH dependence, J. Phys. Chem. B 124 (2020) 3343–3354.
[74] A.P. Lyubartsev, A. Laaksonen, MDynaMix - a scalable portable parallel MD simulation package for arbitrary molecular mixtures, Comput. Phys. Commun. 128 (2000) 565–589.
[75] V. Zoete, M.A. Cuendet, A. Grosdidier, O. Michielin, SwissParam: a fast force field generation tool for small organic molecules, J. Comput. Chem. 32 (2011) 2359–2368.
[76] C.M. Breneman, K.B. Wiberg, Determining atom-centered monopoles from molecular electrostatic potentials. The need for high sampling density in formamide conformational analysis, J. Comput. Chem. 11 (1990) 361–373.
[77] L. Martínez, R. Andrade, E.G. Birgin, J.M. Martínez, PACKMOL: a package for building initial configurations for molecular dynamics simulations, J. Comput. Chem. 30 (2009) 2157–2164.
[78] W.G. Hoover, Canonical dynamics: equilibrium phase-space distributions, Phys. Rev. A 31 (1985) 1695–1697.
[79] M. Tuckerman, B.J. Berne, Reversible multiple time scale molecular dynamics, J. Chem. Phys. 97 (1992) 1990–2001.
[80] U.L. Essmann, L. Perera, M.L. Berkowitz, A smooth particle mesh Ewald method, J. Chem. Phys. 103 (1995) 8577–8593.
[81] M. Brehm, B. Kirchner, TRAVIS - a free analyzer and visualizer for Monte Carlo and molecular dynamics trajectories, J. Chem. Inf. Model. 51 (2011) 2007–2023.
[82] W. Humphrey, A. Dalke, K. Schulten, VMD: visual molecular dynamics, J. Mol. Graph. 14 (1996) 33–38.
[83] T.H. Ibrahim, M.A. Sabri, N.A. Jabbar, P. Nancarrow, Thermal conductivities of choline chloride-based deep eutectic solvents and their mixtures with water: measurement and estimation, Molecules 25 (2020) 3816.
[84] D. Tomida, Thermal conductivity of ionic liquids, in: A. Shahzad (Ed.), Impact of Thermal Conductivity on Energy Technologies, IntechOpen, London, 2018, pp. 17–32.
[85] A. Pandey, R. Rai, M. Pal, S. Pandey, How polar are choline chloride-based deep eutectic solvents? Phys. Chem. Chem. Phys. 16 (2014) 1559–1568.
[86] C. Florindo, A.J.S. McIntosch, T. Welton, L.C. Branco, I.M. Marrucho, A closer look into deep eutectic solvents: exploring intermolecular interactions using solvatochromic probes, Phys. Chem. Chem. Phys. 20 (2018) 206–213.
[87] Y. Cui, C. li, J. Yin, S. Li, Y. Jia, M. Bao, Design, synthesis and properties of acidic deep eutectic solvents based on choline chloride, J. Mol. Liq. 236 (2017) 338–343.
[88] T. El-Achkar, H. Greige-Gerges, S. Fourmentin, Basics and properties of deep eutectic solvents: a review, Environ. Chem. Lett. 19 (2021) 3397–3408.
[89] A. Bakhtyari, R. Haghbakhsh, A.R.C. Duarte, S. Raeissi, A simple model for the viscosities of deep eutectic solvents, Fluid Phase Equil. 521 (2020) 112662.
[90] C.A. Angell, Formation of glasses from liquids and biopolymers, Science 167 (1995) 1924–1935.
[91] A. Kovacs, E.C. Neyts, I. Cornet, M. Wijnants, P. Billen, Modeling the physicochemical properties of natural deep eutectic solvents, ChemSusChem 13 (2020) 3789–3804.
[92] A. Dashti, M. Raji, P. Amani, A. Baghban, A.H. Mohammadi, Insight into the estimation of equilibrium CO_2 absorption by deep eutectic solvents using computational approaches, Separ. Sci. Technol. 56 (2020) 2351–2368.
[93] Z. Yao, Z. Lin, T. Wang, D. Tian, X. Zou, Y. Gao, D. Yin, Using molecular docking-based binding energy to predict toxicity of binary mixture with different binding sites, Chemosphere 92 (2013) 1169–1176.
[94] U. Koch, P.L.A. Popelier, Characterization of C-H-O hydrogen bonds on the basis of charge density, J. Phys. Chem. 99 (1995) 9747–9754.
[95] A. Luzar, Resolving the hydrogen bond dynamics conundrum, J. Chem. Phys. 113 (2000) 10663–10675.
[96] M. Brehm, H. Weber, M. Thomas, P. Holloczki, B. Kirchner, Domain analysis in nanostructured liquids: a post-molecular dynamics study at the example of ionic liquids, ChemPhysChem 16 (2015) 3271–3277.